Binding of heavy metal ions in aggregates of microbial cells, EPS and biogenic iron minerals measured *in-situ* using metal- and glycoconjugates-specific fluorophores

Likai Hao [a,*], Yuan Guo [a], James M. Byrne [b], Fabian Zeitvogel [a], Gregor Schmid [a], Pablo Ingino [a], Jianli Li [c], Thomas R. Neu [d], Elizabeth D. Swanner [e], Andreas Kappler [b], Martin Obst [f,*]

[a] *Environmental Analytical Microscopy, Center for Applied Geosciences, Eberhard Karls University Tübingen, Hölderlinstr. 12, 72074 Tübingen, Germany*
[b] *Geomicrobiology, Center for Applied Geosciences, Eberhard Karls University Tübingen, Hölderlinstr. 12, 72074 Tübingen, Germany*
[c] *College of Chemistry & Materials Science, Northwest University, 710069 Xi'an, Shaanxi, PR China*
[d] *Department of River Ecology, Helmholtz Centre for Environmental Research – UFZ, Brueckstrasse 3A, 39114 Magdeburg, Germany*
[e] *Geobiology, Department of Geological and Atmospheric Sciences, Iowa State University, Ames, IA 50011, USA*
[f] *Bayreuth Center of Ecology and Environmental Research, University of Bayreuth, Dr.-Hans-Frisch-Str. 1-3, 95448 Bayreuth, Germany*

Abstract

Aggregates consisting of bacterial cells, extracellular polymeric substances (EPS) and Fe(III) minerals formed by Fe(II)-oxidizing bacteria are common at bulk or microscale chemical interfaces where Fe cycling occurs. The high sorption capacity and binding capacity of cells, EPS, and minerals controls the mobility and fate of heavy metals. However, it remains unclear to which of these component(s) the metals will bind in complex aggregates. To clarify this question, the present study focuses on 3D mapping of heavy metals sorbed to cells, glycoconjugates that comprise the majority of EPS constituents, and Fe(III) mineral aggregates formed by the phototrophic Fe(II)-oxidizing bacteria *Rhodobacter ferrooxidans* SW2 using confocal laser scanning microscopy (CLSM) in combination with metal- and glycoconjugates-specific fluorophores. The present study evaluated the influence of glycoconjugates, microbial cell surfaces, and (biogenic) Fe(III) minerals, and the availability of ferrous and ferric iron on heavy metal sorption. Analyses in this study provide detailed knowledge on the spatial distribution of metal ions in the aggregates at the sub-μm scale, which is essential to understand the underlying mechanisms of microbe–mineral–metal interactions. The heavy metals (Au^{3+}, Cd^{2+}, Cr^{3+}, CrO_4^{2-}, Cu^{2+}, Hg^{2+}, Ni^{2+}, Pd^{2+}, tributyltin (TBT) and Zn^{2+}) were found mainly sorbed to cell surfaces, present within the glycoconjugates matrix, and bound to the mineral surfaces, but not incorporated into the biogenic Fe(III) minerals. Statistical analysis revealed that all ten heavy metals tested showed relatively similar sorption behavior that was affected by the presence of sorbed ferrous and ferric iron. Results in this study showed that in addition to the mineral surfaces, both bacterial cell surfaces and the glycoconjugates provided most of sorption sites for heavy metals. Simultaneously, ferrous and ferric iron ions competed with the heavy metals for sorption sites on the organic compounds. In summary, the information obtained by the present approach using a microbial model system provides important information to better understand the interactions between heavy metals and biofilms, and microbially formed Fe(III) minerals and heavy metals in complex natural environments.

* Corresponding authors. Tel.: +49 921 55 5703; fax: +49 921 55 5709.
  E-mail addresses: likai.hao@uni-tuebingen.de, likaih2004@126.com (L. Hao), martin.obst@uni-bayreuth.de (M. Obst).

1. INTRODUCTION

Over a billion tons of toxic heavy metals (i.e. Cr, Co, Ni, Cu, Zn, As, Cd, Hg, and Pb) have been released into the environment over the last 30 years (Haferburg and Kothe, 2012), due to anthropogenic activities (Pacyna et al., 2007). Once released into the environment, the mobility and fate of heavy metals is controlled by a suite of linked physical, chemical and microbiological processes. However, microbial activity and metal behavior influence each other, reflecting the physical overlap of microbial habitats and reactive metal zones in the environment (Warren and Haack, 2001). In such heterogeneous, complex systems it is often challenging to unambiguously identify binding and sorption sites and mechanisms for heavy metal species. Previous studies revealed the heterogeneous spatial distribution of heavy metals at the 100 µm scale in a biofilm but further spatial resolution is lacking (Teitzel and Parsek, 2003). Furthermore, imaging and quantifying the *in-situ* spatial relationships of glycoconjugates, microbial cell surfaces, and (biogenic) minerals, while simultaneously accounting for the contribution of these components to heavy metals sorption has proven difficult due to sample disturbance during preparation. However, detailed knowledge on the spatial distribution of heavy metal species in aggregates and biofilms on the sub-µm scale is essential to understand the contribution of microbe–mineral–metal interactions to heavy metal sorption.

Various analytical microscopy approaches can be used for quantitatively studying the distribution of heavy metals in chemically fixed biological specimens (Denkhaus et al., 2007). However, analytical (electron) microscopy studies of cell-EPS-Fe(III)-mineral aggregates and biofilms are experimentally challenging, as these complex and heterogeneous systems contain both soft organic matter and mineral phases that are easily affected by artifacts from sample preparation. Dehydration and critical point drying (CPD) or embedding procedures often involve various types of solvents and chemicals that can alter the distribution and concentration of the chemical constituents (Chang and Rittmann, 1986; Schädler et al., 2008), and consequently alter the native heavy metal sorption. Thus samples are best studied under natural, hydrated conditions using an appropriate nondestructive, noninvasive approach such as scanning transmission X-ray microscopy (STXM) (Kemner et al., 2005; Templeton and Knowles, 2009), or confocal laser scanning microscopy (CLSM) (Hao et al., 2013).
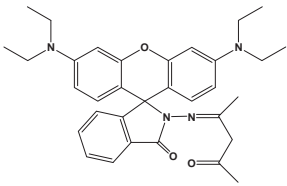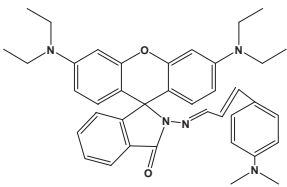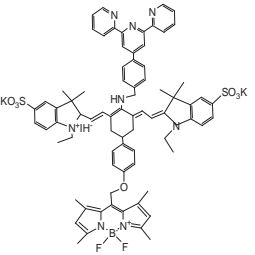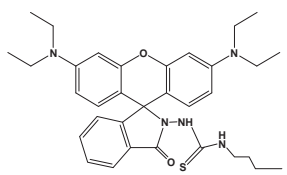
CLSM is a powerful tool for *in-situ* deciphering the 3D structure, composition, dynamics, and reactivity of biofilms (Bridier and Briandet, 2014; Neu and Lawrence, 2014a,b). For example, coupled with fluorescence lectin-binding analysis (FLBA), it has been used to study the functional group composition of glycoconjugates in microbial aggregates and biofilms (Neu and Lawrence, 1999, 2003). It also has been used to map the spatial distribution of metals in biofilms (McLean et al., 2008), to localize the spatial distribution of Zn^{2+} and active biomass in biofilms (Hu et al., 2005), to evaluate the effect of Ni^{2+} on a natural river biofilm (Lawrence et al., 2004), and to determine the heterogeneous distribution of Ni^{2+}, Zn^{2+}, Fe^{3+} and Cd^{2+} in various
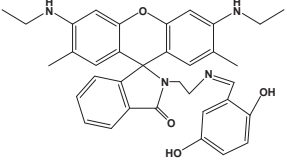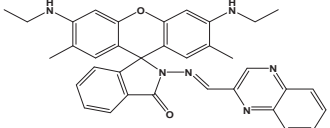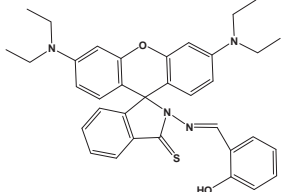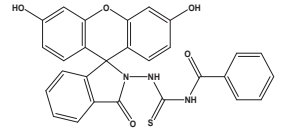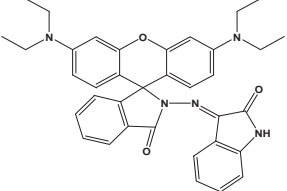
biofilms (Wuertz et al., 2000; Ueshima et al., 2008; Shumi et al., 2009), using relatively poorly selective, commercially available metal fluorescence probes. Other studies used CLSM to show the heterogeneity of physicochemical microenvironments in complex natural biofilms (Zhang et al., 2011b; Reuben et al., 2014) and to measure pH with specific pH-dependent fluorescent indicators in biofilms (Hunter and Beveridge, 2005), and around Fe(II)-oxidizing bacteria *in-situ* (Hegler et al., 2010), in microbial biofilms by silica nanoparticle sensors (Hidalgo et al., 2009). However, almost all studies were limited to imaging cells or extracellular polymers (Chen et al., 2006, 2007), or rather focused on the diversity and abundance of microbial species, cell activity, and the composition of extracellular polymeric substances (Halan et al., 2012). Because of a lack of applicable, highly sensitive and selective metal fluorescent probes (Marx, 2013), metal distributions in wet environmental samples have rarely been studied by CLSM until recently. The development of highly selective and sensitive metal fluorescence probes in the last years has allowed for studying local heavy metal distributions and concentrations in bacterial microenvironments (Hao et al., 2013; Wessel et al., 2013; Schmid et al., 2014; Wu et al., 2014).

Many of these probes can be used for microscopic metal localization in biological samples in combination with fluorescence microscopy or CLSM (Nagano, 2010; Dean et al., 2012; Vendrell et al., 2012; Yang et al., 2012). These compounds therefore represent a novel possibility for *in-situ* imaging of heavy metals sorbed to the cell surface, glycoconjugates, and biomineral components. Therefore, in this study, novel, metal-specific, metal-induced rhodamine spirolactam ring-opening 'turn-on'-type fluorescent probes (Beija et al., 2009; Yang et al., 2012) were screened (Table 1). The strategies of how to select particularly specific and sensitive metal fluorescence probes for environmental research and in particular to map the distribution of various heavy metal species such as Au^{3+}, Cd^{2+}, Cr^{3+}, CrO_4^{2-}, Cu^{2+}, Fe^{2+}, Fe^{3+}, Hg^{2+}, Ni^{2+}, Pd^{2+}, TBT and Zn^{2+} in cell-EPS-Fe(III)-minerals aggregates and biofilms are discussed. These probes were used to map metal species and compared the distribution to other constituents of cell-EPS-Fe(III)-mineral aggregates formed by the anoxygenic, phototrophic Fe(II)-oxidizing bacteria *Rhodobacter ferrooxidans* strain SW2 as a proof-of-concept. The present study detailed how spectral overlaps in both excitation and the emission spectra can be minimized during simultaneous staining of bacterial cells, metals, and glycoconjugates. Here a labeling scheme using Syto 40® or Syto 9® for labeling DNA of bacterial cells, rhodamine 6G and rhodamine B as the fluorophore in probes for labeling heavy metal species, and Lectin-Alexa Fluor conjugates (Table 2) for labeling glycoconjugates was developed (Hao et al., 2013; Schmid et al., 2014; Wu et al., 2014). Various statistical analysis approaches, namely correlation analysis, were used on the resulting multi-dimensional datasets to determine the differences in sorption behavior of the metal species. Thus, the results of this study provide an important basis of understanding that will help for predicting the stability of heavy metals sorption under varying environmental conditions: They describe – under *in-situ* conditions – the
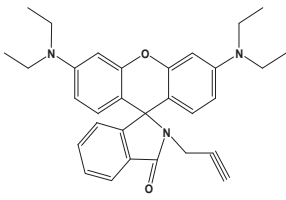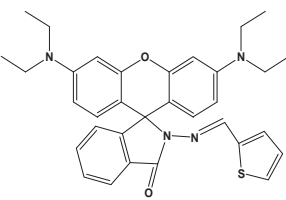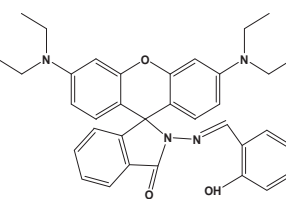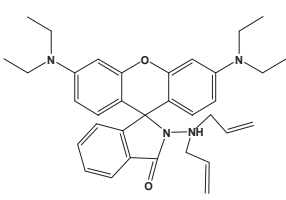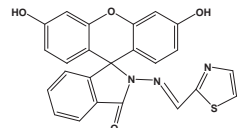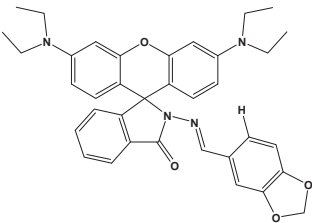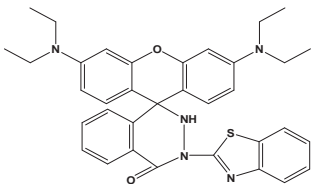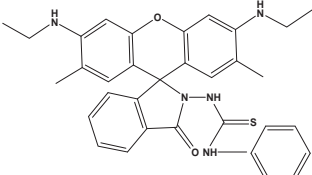
Table 1
Specific metal fluorescent probes that were used in the staining scheme.

Me[a]	Chemical formula	Fluorophore	Linker	RY[b] (%)	Ex[c] (nm)	Em[d] (nm)	DL[e] (μM)	DR[f] (μM)	Solvent[g]	References
Fe^{3+}		Rhodamine B	Acetylacetone	84	570	592	0.004 μM	0.5–50 μM	EtOH-H_2O	Zhang et al. (2011a)
Fe^{2+}		Rhodamine B	N,N-dimethylaminocinnamaldehyde	78	470	582	0.060 μM	0–20 μM	THF-H_2O	Kumar et al. (2011)
Fe^{2+a}		BODIPY cyanine	4′-(amino-methylphenyl)-2,2′,6′,2″-terpyridine	10	569	635	0.012 μM	0.1–7 μM	HEPES	Li et al. (2011)
Cu^{2+}		Rhodamine B	n-Butyl isothiocyanate	68	510	580	0.16 μM	0.08–2.5 μM	CH_3CN-HEPES	Yu et al. (2008)

Ion	Fluorophore	Recognition group							Reference
Cu[2+bc]	Rhodamine 6G	2,4-dihydroxybenzaldehyde	90	480	545	0.1 μM	0.05–5 μM	HEPES	Xi et al. (2010)
Cu[2+bc]	Rhodamine 6G	2-acetyl-(1,4)-benzodiazine	80	520	545	0.04 μM	0.5–1 μM	PBS	Yu et al. (2009)
Zn^{2+}	Rhodamine B	Salicylaldehyde	70	560	590	0.04 μM	0.2–20 μM	CH₃CN-HEPES	Han et al. (2010)
Zn[2+b]	Fluorescein	Benzoylthiourea	60	490	528	0.002 μM	0–50 μM	CH₃CN-H₂O	Yang et al. (2015)
Cd^{2+}	Rhodamine B	2,3-indolinedione	63	563	582	0.5 μM	1–20 μM	MeOH-H₂O	Xu et al. (2012)

(*continued on next page*)

Au^{3+}		Rhodamine B	Prop-2-yn-1-amine	92	558	579	0.5nM	0.5–4 µM	EtOH-H$_2$O	Jung Jou et al. (2009)
Cr^{3+}		Rhodamine B	Thiophene-2-furanaldehyde	81	510	583	0.5 µM	0.5–8 µM	CH$_3$CN	Weerasinghe et al. (2009)
CrO$_4^{2-}$		Rhodamine B	Salicylaldehyde	55	520	591	0.0015 µM	0.01–0.3 µM	H$_2$O	Zheng et al. (2009)
Pd^{2+}		Rhodamine B	3-Bromopropene	45	530	580	0.185 µM	0.094–1 µM	EtOH-H$_2$O	Li et al. (2010)
Ni^{2+}		Fluorescein	Thiazole-2-carbaldehyde	75	470	515	2 µM	4–20 µM	DMSO-H$_2$O	Abebe et al. (2011)

TBT		Rhodamine B	Piperonyl aldehyde	78	558	577	0.25 μM	6–20 μM	CH$_3$CN-PBS	Jin et al. (2015)
Hg^{2+}		Rhodamine B	2-Hydrazinobenzothiazole and triethylamine	22	550	574	0.03 μM	0.03–20 μM	EtOH-PBS	Yang et al. (2013a)
Hg^{2+bc}		Rhodamine 6G	Thiosemicarbazide	20	500	557	0.4 μM	0.1–12 μM	PBS	Ko et al. (2006)

[a] Me: metal; Fe^{2+a} probe and Me^{2+bc} probes were used for triple metal ion labeling, Me^{2+b} probes were used for dual metal ion labeling.
[b] RY: reaction yield.
[c] Ex: excitation.
[d] Em: emission.
[e] DL: detection limit.
[f] DR: detection range.
[g] MeOH: methanol, EtOH: ethanol, THF: tetrahydrofuran, CH$_3$CN: acetonitrile, HEPES: 4-(2-hydroxyethyl)-1-piperazineethanesulfonic acid, PBS: phosphate buffered saline, DMSO: dimethyl sulfoxide, H$_2$O: water.

Table 2
The stains used in the staining scheme.

Fluorescent probes	LW[a] (nm)	SDR[b] (nm)	Ex[c] (nm)	Em[d] (nm)	Targets
SYTO® 9 Green	488	496–560	485	498	Total cells nucleic acids
SYTO® 40 Blue	405	415–475	420	441	Total cells nucleic acids
Con A Conjugates, Alexa Fluor® 488	488	496–560	495	519	α-Mannopyranosyl,α-glucopyranosyl residues
PNA Conjugates, Alexa Fluor® 568	561	570–620	579	603	Terminal β-galactose
PNA Conjugates, Alexa Fluor® 647	635	640–700	650	668	Terminal β-galactose
SBA Conjugates, Alexa Fluor® 647	635	640–700	650	668	Terminal α- and β-N-acetylgalactosamine and galactopyranosyl residues
SBA Conjugates, Alexa Fluor® 488	488	496–560	495	519	Terminal α- and β-N-acetylgalactosamine and galactopyranosyl residues
WGA Conjugates, Alexa Fluor® 555	561	570–620	555	565	N-acetylglucosamine and N-acetylneuraminic acid residues
WGA Conjugates, Alexa Fluor® 633	635	640–700	632	647	N-acetylglucosamine and N-acetylneuraminic acid residues

[a] LW: laser wavelength used in this study.
[b] SDR: spectra detection range used in this study.
[c] Ex: excitation maximum.
[d] Em: emission maximum.

partitioning of various heavy metal species between biogenic and organic and inorganic sorbents. As these react differently to changes in pH (e.g. deprotonation of functional groups), redox state or metal concentrations (e.g. affecting the excretion EPS by bacteria), this fundamental understanding of the partitioning is essential.

2. MATERIALS AND METHODS

2.1. Medium and bacterial culture

An anoxic, freshwater, minimal-salts medium with a phosphate concentration of 1 mM was prepared according to (Hegler et al., 2008). Sterilized vitamins and trace-element solutions (1 mL each per liter) were added to the medium after autoclaving. The medium contained sodium bicarbonate (22 mM) in equilibrium with a headspace of N_2–CO_2 (80:20) introduced immediately after autoclaving to keep the medium anoxic. The pH was adjusted to 6.8 using additions of anoxic 1 N HCl or 1 M $NaCO_3$. When *R. ferrooxidans* SW2 was cultivated with Fe(II) as electron donor, $FeCl_2$ was added from an anoxic stock bottle (10 mM) to the medium and left to precipitate any Fe(II) carbonate or phosphate minerals for 48 h at room temperature. The medium was then filtered through 0.22 μm Millipore filters in an anoxic glove box (100% N_2). After filtration, the medium contained a final concentration ca. 4.5–6 mM dissolved Fe(II) and approximately 10−20 μM phosphate (Kappler et al., 2010). One percent (vol.) of a preculture in stationary phase that had been grown on H_2 as an electron donor (Croal et al., 2007) was used as the inoculum for the Fe(II)-oxidizing culture. Cultures were incubated at 20 °C under continuous illumination. For CLSM analyses, 10-day old aliquots of the same culture were sampled under anoxic conditions (Miot et al., 2009).

For mineralogical analysis, 180-day old of the same culture were sampled under anoxic conditions.

2.2. Confocal laser scanning microscopy (CLSM)

Image stacks (512 × 512 pixels) were acquired in sequential mode using an upright Leica TCS SPE system with an ACS APO 63× water immersion CS objective (NA: 1.15) (Leica Microsystems, Wetzlar, Germany). The CLSM was equipped with four solid state lasers (405, 488, 561, and 635 nm). Staining schemes and instrument settings used in this study are summarized in Tables 2 and 3. The reflection signal was recorded using the 488 nm laser and a detection wavelength range of 485–495 nm. Frame averaging of 3–6 frames was used to reduce noise and to improve image quality. Images of different channels were obtained sequentially (Clarke et al., 2010; Hao et al., 2013). The pinhole was set to 0.5 Airy units (77.5 μm for the 63× lens, NA = 1.15) to optimize lateral and axial resolution at the cost of signal intensity. Z-stacks were acquired over a depth of 3.2 μm using a step-size of 0.08 μm. Three to five image stacks were acquired with the same settings. Triplicate measurements of each sample type were used for the subsequent quantitative data analysis.

2.3. Fluorescent probes preparation

Selective metal chelators are linked to rhodamine to form nonfluorescent lactam molecules under acidic conditions (Nguyen and Francis, 2003). Thereby the spirolactam or spironolactone ring creates a specific metal ion binding site (Hao et al., 2013). All the following probes used rhodamine B as fluorescent reporter and lactam as turn-on switch of the fluorescence. All probes have a common detection mechanism. The presence of the target metal

triggers the ring-opening of the corresponding spirolactam/lacton resulting in a strong rise of fluorescence emission upon excitation with the appropriate wavelength of visible light. This allows for visualization of the metal distribution in cell-EPS-Fe(III)-minerals aggregates on the submicrometre scale (Hao et al., 2013).

Rhodamine B lactam was synthesized by dropwise addition of 5 mL phosphorus oxychloride to a stirred solution of 0.01 mol rhodamine hydrochloride in 10 mL of 1,2-dichloroethane. Afterwards it was refluxed for 6 h, then concentrated by evaporation. Finally the crude acid chloride obtained was dissolved in 10 mL acetonitrile (She et al., 2012; Yang et al., 2013b). The specific linkages used for each metal are described below. After synthesis of each sensor, all the crude products were purified twice by column chromatography. The final products were confirmed by absorbance spectroscopy (Shimadzu UV-1700 spectrophotometer) and fluorescence spectroscopy (HITACHI F-4500 fluorescence spectrophotometer), while the molecular structures were confirmed based on their NMR spectra (Varian INOVA-400 MHz spectrometer, 400 MHz for ^{1}H NMR and 100 MHz for ^{13}C NMR) with tetramethylsilane as reference (She et al., 2012; Yang et al., 2013b). All metal fluorescent probes used in this study are summarized in Table 1. An Fe^{2+} fluorescent probe emitting in the far red (BDP-Cy-Tpy) was kindly provided by Prof. B. Tang.

The nucleic acid stains SYTO® 9 Green and SYTO® 40 Blue (Molecular Probes, Inc.) were used to visualize the bacterial cells in the cell-EPS-Fe(III)-mineral aggregates. To stain the extracellular glycoconjugates in these cell-EPS-Fe(III)-mineral aggregates, four different lectins conjugates to various Alexa Fluor® dyes (Molecular Probes, Inc.) were used; these were Concanavalin A conjugates, PNA conjugates, SBA conjugates and WGA conjugates.

2 mM metal fluorescent probe stock solutions were prepared using pure acetone or DMSO, and stored in the dark at 4 °C. Stock solutions of the commercially available SYTO® fluorescent nucleic acid stains and the far-red fluorescence Alexa Fluor® conjugates were stored frozen at −25 °C and thawed prior to staining.

2.4. Staining procedure

For metal sorption experiments, bacterial samples in the stationary phase were incubated with 5 μM of the individual heavy metals for 1 h. This concentration was tested to be within the linear range of the theoretical polarographic titration curve (Comte et al., 2008). The samples were then incubated with 5–10 μM of the individual metal fluorescent probes for 3 h at 20 °C prior to analysis in the CLSM. Samples treated with 0.01 M EDTA were used as negative controls, as this concentration effectively removes residual heavy metals such as Cu^{2+}, Zn^{2+}, Pb^{2+} and Cd^{2+} on bacterial surfaces and within the EPS (mainly composed of glycoconjugates) without affecting the cell activity (Cox et al., 1999). For bacteria staining, the SYTO® dyes were diluted 1:1000 using sterilized Milli-Q water. The amounts of the resulting working solution that were added to the

samples were adjusted according to the cell numbers. Usually SYTO® 40 was used for multiple metal labeling and SYTO® 9 was used for single metal labeling to avoid overlap of the emission spectra of the individual dyes. For glycoconjugate labeling, lectin Alexa Fluor® conjugate solutions were diluted 1:10 and then added to the samples in small volumes that were adjusted according to the lectin Alexa Fluor® conjugate fluorescent intensity present in the sample. Two to three microliter of the sample were pipetted onto a clean microscopic slide in the center of a 9 mm × 0.12 mm SecureSeal™ imaging spacer (Grace Bio-Labs, PolyAn GmbH, Germany) and a cover slip was placed on top of the droplet. The edges of the cover slip were sealed with transparent nail polish to avoid dehydration of the CEMA specimens and to avoid the oxidation of residual Fe^{2+} in the glovebox which would lead to artifacts, such as shrinkage or aggregation. This preparation of samples in their natural, hydrated state allows for accurate in-situ CLSM studies of the aggregates/biofilm structure (Bar-Zeev et al., 2014).

In order to quantitatively compare the amount of metal ions bound to the cell surface, to the glycoconjugates, and to the biogenic Fe(III) minerals, the native samples were compared to samples that either had the glycoconjugates removed by enzymatic digestion, or in which the Fe(III) minerals were removed by reductive dissolution as described in detail in the following sections.

2.5. Development of a staining procedure for multiple metal species labeling

In this study, a staining procedure was developed for studying cell-EPS-Fe(III)-mineral aggregates, biofilms or environmental samples using multiple probes for various organochemical components and metal fluorescence probes simultaneously. Therefore, such probes needed to fulfill the following general requirements. They should be stable at circumneutral pH or within the pH-range of the sample that is studied, and within the desired temperature range. As the chemical sample environment is complex, they need to be as specific and selective as possible. Furthermore, they should respond quickly and need to be excitable with the wavelengths that are available at the CLSM that is used for the analysis; most versatile is an excitation within the visible light wavelength range as this does not require any special optics. For studying the distribution of a compound in heterogeneous environments, turn-on type probes that show an increasing fluorescence with increasing compound concentration are advantageous. Additionally, all the fluorescence probes should be resistant against photobleaching (Rosivatz, 2008). To prevent cross talk between the individual emission channels, fluorescence probes with separate excitation and emission spectra were selected (Fig. S1) and a multiple fluorescent probe staining scheme is proposed. Hardware limitations of the CLSM, such as the available laser excitation wavelength, a conventional vs. acousto-optical beam splitter, and a filter-based vs. wavelength-adjustable detection beampath have to be

Table 3
The stains used in the staining scheme.

Fluorescent probes	LW[a] (nm)	SDR[b] (nm)	Ex[c] (nm)	Em[d] (nm)	Targets
Single metal fluorescence labeling schedule					
SYTO® 9 Green	488	496–560	485	498	Total cells nucleic acids
Rhodamine B based metal probe	561	570–620	560	580	Relevant metal ions
WGA Conjugates, Alexa Fluor® 633	635	640–700	632	647	N-acetylglucosamine and N-acetylneuraminic acid residues
Dual-metal fluorescence labeling schedule					
SYTO® 40 Blue	405	415–475	420	441	Total cells nucleic acids
Rhodamine 6G based metal probe	488	496–560	500	545	Relevant metal ions
Rhodamine B based metal probe	561	570–620	560	580	Relevant metal ions
WGA Conjugates, Alexa Fluor® 633	635	640–700	632	647	N-acetylglucosamine and N-acetylneuraminic acid residues
Tri-metal fluorescence labeling schedule					
SYTO® 40 Blue	405	415–475	420	441	Total cells nucleic acids
Rhodamine 6G based metal probe	488	496–560	500	545	Relevant metal ions
Rhodamine B based metal probe	561	570–620	560	580	Relevant metal ions
Fluorescent probes for Fe (II) 2	561	640–700	569	635	Fe (II) metal ions

[a] LW: laser wavelength used in this study.
[b] SDR: spectra detection range used in this study.
[c] Ex: excitation maximum.
[d] Em: emission maximum.

considered when designing a multiple fluorescent probe staining scheme. Details of the schemes used in this study are listed in Table 3. Seventeen metal fluorescent probes were selected from more than 1000 reported candidates.

2.6. Glycoconjugates enzymic digestion

Glucoamylase was used for enzymatic digestion of the glycoconjugates. This enzyme specifically and effectively breaks the α-1,4-glucosidic bonds within EPS (Ueshima et al., 2008) of *R. ferrooxidans* SW2. To preserve the bacterial cell integrity, and to avoid unpredictable disruption of the aggregate components by the various steps of treatment, the following protocol was devised. Approximately 4 mL of bacterial culture in stationary phase was suspended in twenty units (i.e. amount of the enzyme necessary to catalyze a conversion of 1 μM per minute) of glucoamylase (USBio, highly purified, Biomol GmbH) in 16 mL of sterilized 0.1 M NaClO$_4$ solution. The cell suspension was incubated at 30 °C for 12 h while it was gently shaken (Ueshima et al., 2008). Then suspensions were centrifuged (1000g) and washed three times with sterilized freshwater minimal-salts medium with a phosphate concentration of 1 mM. Finally the glycoconjugates-digested sample was resuspended in 4 mL freshwater minimal-salts medium. Untreated and enzyme-treated samples were imaged under the same conditions in the CLSM after lectin staining to determine the extent of glycoconjugates removal.

2.7. Fe(III) oxyhydroxide digestion by oxalate solution

Fe(III) oxyhydroxides such as ferrihydrite or goethite can be dissolved within 10 min in the presence of Fe^{2+} using a mixture of ammonium oxalate/oxalic acid (Suter et al., 1988). Five milliliter of the bacterial culture in the stationary phase following Fe(II) oxidation was fixed by 1 mL 20% paraformaldehyde for 30 min. Then, 4.5 mL of oxalate solution (100 mM ammonium oxalate and 83 mM oxalic acid) and 0.1 mL of a filtered, anoxic solution of 100 mM ferrous ethylenediammonium sulfate (as an Fe^{2+} source) were added and gently shaken (10 min) until all Fe-mineral precipitates were dissolved. The suspensions were centrifuged (1000g) and washed three times with sterilized freshwater minimal-salts medium with a phosphate concentration of 20 μM. Finally, the Fe(III) mineral-free samples were resuspended in 5 mL freshwater minimal salts medium. Untreated and oxalate-treated samples were imaged under the same conditions in the CLSM to determine the extent of Fe(III) mineral removal.

2.8. Data treatment and digital image analysis

Blind deconvolution was applied to all 3D image stacks using the Auto-Quant™ deconvolution algorithm implemented in the LEICA LAS AF software (Schmid et al., 2014). Fiji based on ImageJ 1.49b (http://fiji.sc/Fiji) (Abramoff, 2004) was used for data handling, visualization and quantification. Scatterplots for correlation analysis were created using the ImageJ plugin ScatterJ (Zeitvogel et al., 2014).

For an efficient quantitative analysis of the comprehensive 3D datasets, the software tool JImageAnalyzer (Version 1.4, UFZ-Umweltforschungszentrum Leipzig-Halle GmbH), which is also based on ImageJ (http://imagej.nih.gov/ij/) (Wagner et al., 2009, 2010a; Buchholz et al., 2012) was used. A fluorescence intensity threshold was selected for each individual image stack to separate signal from background noise. This resulted in a stack of binary images where values of 1 represent the foreground signal and 0 as the background signal. Foreground pixels representing glycoconjugates, heavy metal species and cells (DNA) were counted to calculate the total pixels (pixel size

0.03 μm × 0.03 μm), which represented the total volume of glycoconjugates, heavy metal species and cells (DNA) within the respective sample volume. To ensure comparability, this procedure was done by the same operator using the same conditions for all analysis (Wagner et al., 2010b).

Here a Pearson's correlation coefficient was used to quantitatively describe co-localization (Adler and Parmryd, 2010; Barlow et al., 2010). The fuzzy linguistic system of Zinchuk, V. et al. was used to describe "weak", "moderate" and "strong" co-localization (Zinchuk et al., 2013). On the deconvolved 3D datasets, the co-localization was analyzed quantitatively using the Coloc-module of Imaris 7.7.2 (Bitplane, Zurich, Switzerland) and the ImageJ plugin JACoP (Just Another Colocalization Plugin) provided by Bolte and Cordelieres (2006). Pixel co-distributions were calculated from sets of two fluorescence signals in the entire 3D volume of each dataset, which then enables the user to distinguishing between colocalization and a random association between these signals. From these datasets, the Pearson's correlation coefficient (without threshold) and the percentages of colocalized volumes (data collected from Imaris, not shown) were calculated (Staudt et al., 2004; Zippel and Neu, 2011).

Principal components analysis (PCA, Pearson matrix was used) was performed on triplicate experiments using XLSTAT (Version 2014.6.01, Addinsoft, New York, NY, USA). The proximity of heavy metals species and the bacteria or glycoconjugates in the biplot indicate the correlation strength. To further confirm the PCA grouping result, a heatmap analysis was done using the clustergram software package of Matlab v. R2012a (Zheng et al., 2014).

2.9. Micro X-ray diffraction and ^{57}Fe Mössbauer spectroscopy

Micro X-ray diffraction (μXRD) analysis was carried out on dried mineral samples (in anoxic glovebox, 100% N_2), which were mounted onto a Si single crystal silicon

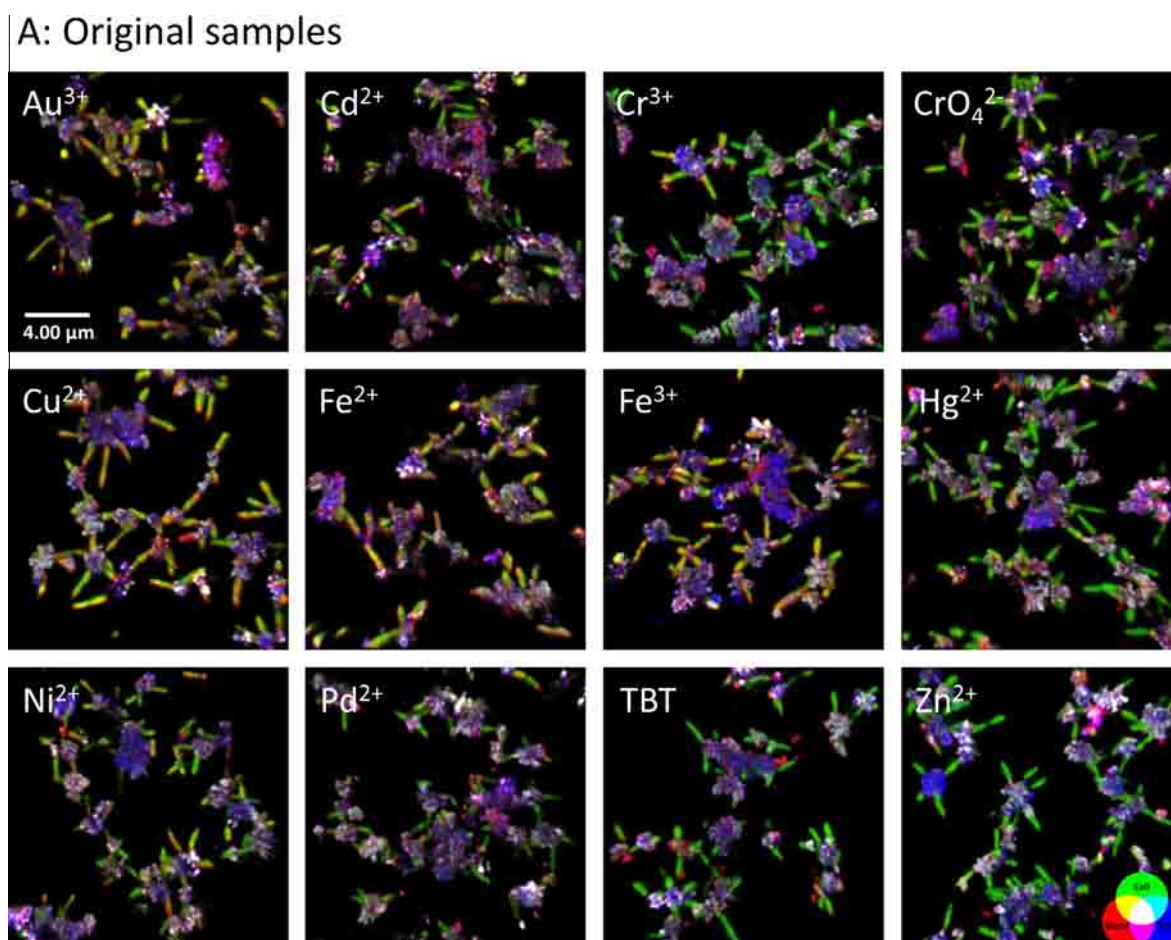Fig. 1. 2D maximum intensity projections of multiple channels of 3D data sets from CLSM illustrating the sub-μm scale composition of cell-EPS-Fe(III)-minerals aggregates with single metal ions labeling. Twelve cultures of the phototrophic Fe(II)-oxidizing *Rhodobacter ferrooxidans* strain SW2 were analyzed, containing Au^{3+}, Cd^{2+}, Cr^{3+}, CrO_4^{2-}, Cu^{2+}, Fe^{2+}, Fe^{3+}, Hg^{2+}, Ni^{2+}, Pd^{2+}, TBT and Zn^{2+}. Cells were stained with SYTO® 40 blue fluorescent nucleic acid stain (green), a probe labeling the respective heavy metal ion added at 10 μM to the culture (red), and the WGA-Alexa Fluor 633 conjugate labeling glycoconjugates (blue) were added. Fe(III) minerals are visualized by using their reflection signal at 488 nm wavelength (gray). Brighter colors indicate higher concentrations. A: Original samples; B: Glycoconjugate digested samples; C: Mineral digested samples. Physical length of each image is 17.46 × 17.46 μm. Scale is the same for all images.
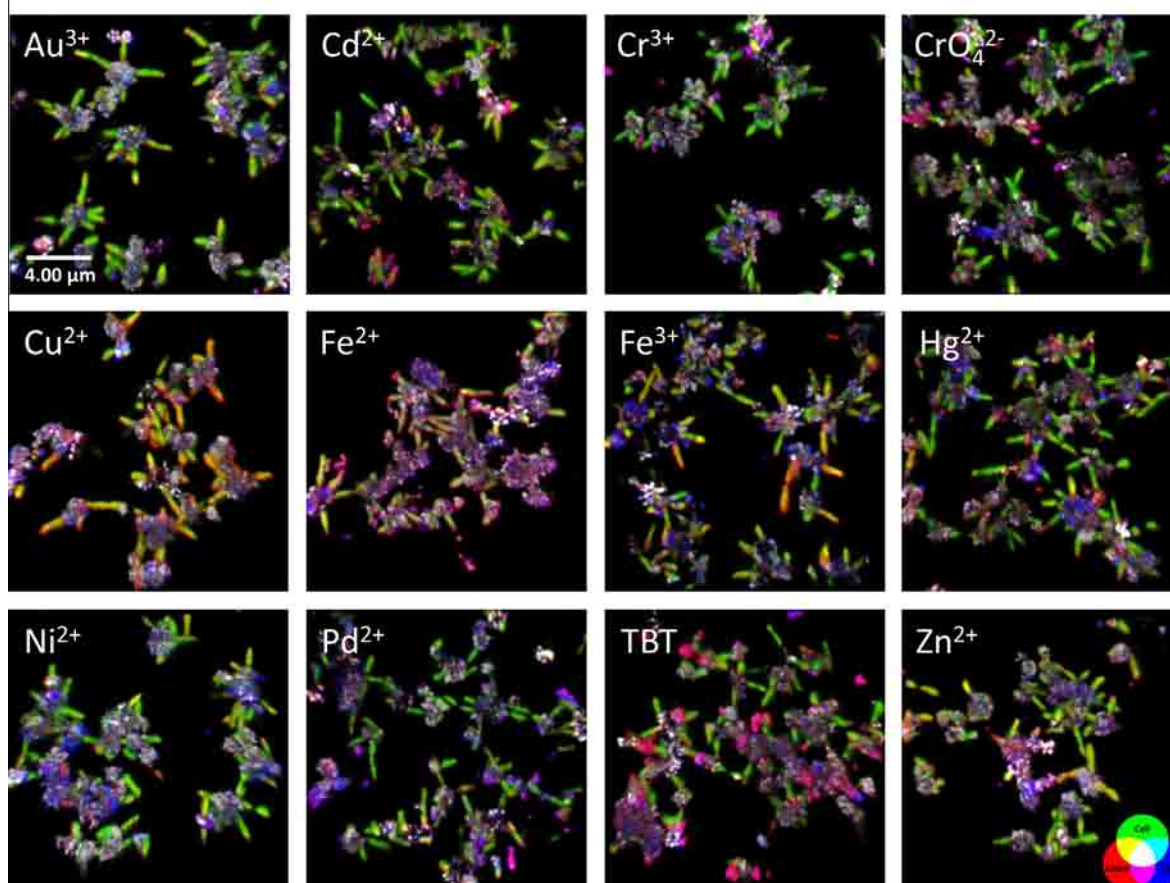
Fig 1. *(continued)*

wafer. Data was collected with a Bruker D8 Discover XRD instrument (Bruker, Germany) using a Co Kα X-ray tube, ($\lambda = 0.17902$ nm, 30 kV, 30 mA) and GADDS area detector (Berthold et al., 2009). Mineral phases were determined by comparison to the database of the International Center for Diffraction Data (ICDD). For ^{57}Fe Mössbauer spectroscopy recorded at 295 K, 77 K and 4.2 K, samples were prepared inside an anoxic glovebox (100% N_2) by passing the suspension containing the Fe-minerals through filter paper (0.44 μm). The filter paper loaded with sample was then sealed between two layers of Kapton tape to create an anoxic seal. Samples were removed from the glovebox and loaded into a close-cycle exchange gas cryostat. The Mössbauer spectrometer (WissEL) was operated in transmission mode, with a ^{57}Co/Rh source driven in constant acceleration. The instrument was calibrated with a 7 μm thick α-^{57}Fe foil measured at room temperature, which was also used to determine the half width at half maximum (fixed to 0.138 mm/s during fitting). Fitting was carried out using Recoil (University of Ottawa) with the extended Voigt based fitting routine (xVBF) (Lagarec and Rancourt, 1997).

3. RESULTS

3.1. Visualizing bio-essential metals and heavy metals

Twelve different heavy metals were stained individually with relevant metal ion fluorescent probes, whereas microbial cells were stained with DNA specific Syto 40® or Syto 9®, and the microbial glycoconjugates were stained with lectin Alexa Fluor® conjugates, which fluoresce in the far-red. The results of the single metal probe images are reported in Fig. 1A, which illustrate the heavy metals Au^{3+}, Cd^{2+}, Cr^{3+}, CrO_4^{2-}, Cu^{2+}, Fe^{2+}, Fe^{3+}, Hg^{2+}, Ni^{2+}, Pd^{2+}, TBT and Zn^{2+} *in-situ* spatial relationships with glycoconjugates, microbial cell surfaces, and (biogenic) minerals in their native states. Most glycoconjugates were found to be segregated and dispersed from the bacterial cells with a distribution pattern similar to those of minerals, indicating a close association of glycoconjugates and the Fe minerals (Fig. 1A). While α-1,4-glucosidic residuals within glycoconjugates are removed by glucoamylase enzymatic digestion, the digestion cannot completely remove the glycoconjugates from the cell-EPS-Fe(III)-minerals aggregates
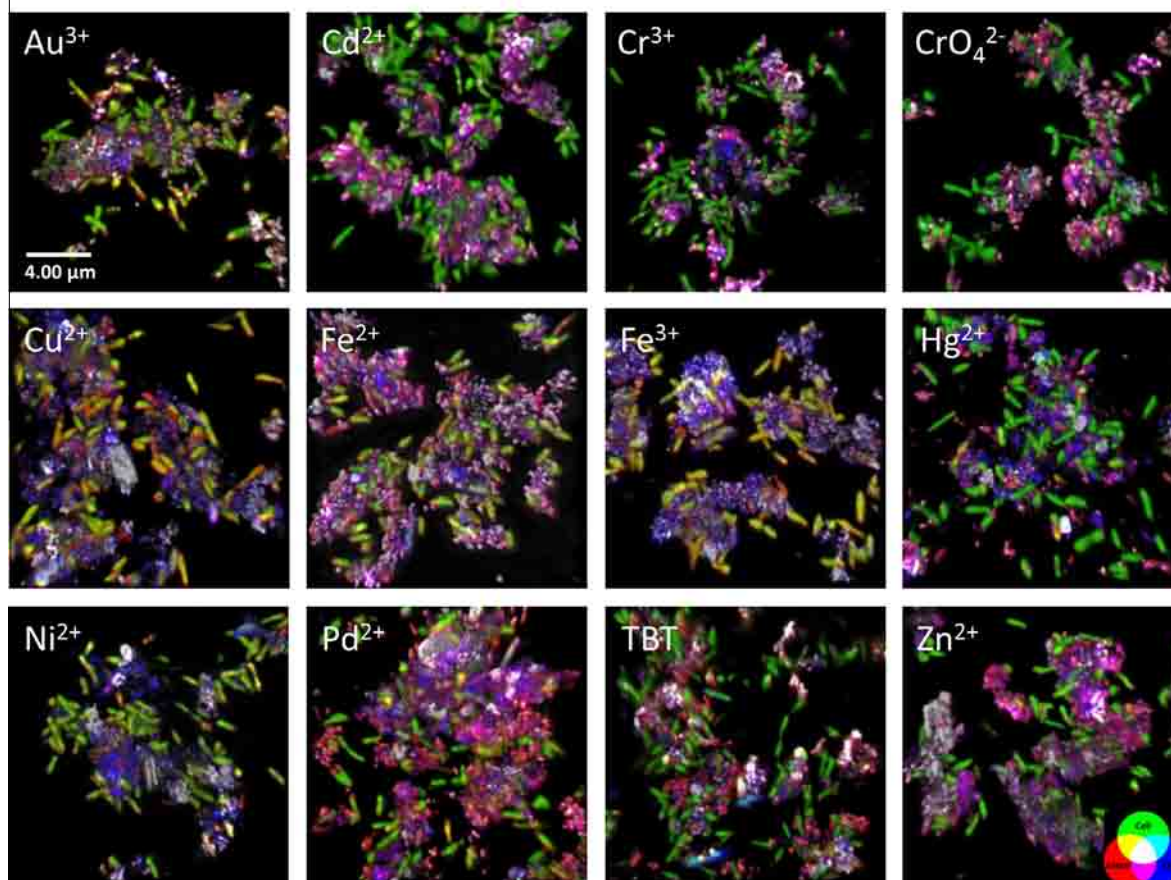
Fig 1. *(continued)*

(Fig. 1B). Instead, digestion led to more heavy metals sorption at the cell surfaces (Fig. 5B). This observation demonstrates that glucoamylase enzymatic digestion did not destroy the intact states of cell-EPS-Fe(III)-minerals aggregates, but only decreased the amount of heavy metals binding sites on glycoconjugates (Figs. 1B, 5A), which are additional sorbents for heavy metals. When Fe(III) oxyhyxdroxides such as ferrihydrite or goethite were removed with a mixture of ammonium oxalate/oxalic acid, heavy metals that were presumably bound to these minerals are accommodated by sorbing to cell surfaces and glycoconjugates (Figs. 1C, 5A and B). Mineral removal caused an increase of the areas covered by cells and glycoconjugates per total analyzed area as compared to the original samples, as shown in the comparison of Fig. 1C and A. All heavy metals were predominantly associated with glycoconjugates and residual mineral in these samples. The areas of all metals associated with both cells and glycoconjugates increased (Fig. 5A, B). In oxalate-digested samples large aggregates formed (Fig. 1C), revealing that the integrity of the initial cell-EPS-Fe(III)-minerals aggregates is lost likely due to chemical changes during oxalate treatment.

Four different heavy metals, Cu^{2+}, Hg^{2+}, Ni^{2+} or Zn^{2+}, stained with the respective green fluorescent probes, and Fe^{2+} and Fe^{3+} stained with relevant red fluorescent probes as well as the DNA specific Syto 40® and lectin Alexa Fluor® conjugates were imaged sequentially for the dual metal-imaging dataset (Fig. 2). Most glycoconjugates were segregated from the bacterial cells and dispersed. The minerals showed the same distribution pattern as in Fig. 1, again indicating a close association of glycoconjugates and the Fe minerals (Fig. 2). Furthermore, triple metal ion labeling with Fe^{2+}, Fe^{3+} and Cu^{2+} or Hg^{2+} in combination with DNA specific Syto 40® blue for staining the bacterial cells show very similar results (Fig. 3).

When *R. ferrooxidans* SW2 was grown under increasing Fe^{2+} (as electron donor) concentrations, a corresponding increase in the amount of glycoconjugates present in cell aggregates was observed (Fig. 4A). This was accompanied by Fe^{3+} complexation to glycoconjugates, and the formation of Fe(III) minerals. Cell-EPS-Fe(III)-minerals aggregates also increased in size with increasing Fe(II) concentration (Fig. 4A). In contrast to cultures of *R. ferrooxidans* SW2 where H_2 was the electron donor,

Fig. 2. 2D maximum intensity projections of multiple channels of 3D data sets from CLSM illustrating the sub-μm scale composition cell-EPS-Fe(III)-minerals aggregates with dual metal ions labeling. Four cultures of the phototrophic Fe(II)-oxidizer *Rhodobacter ferrooxidans* strain SW2 were analyzed, containing either Cu^{2+}, Hg^{2+}, Ni^{2+} or Zn^{2+}. Cells were stained with SYTO® 40 blue fluorescent nucleic acid stain (green A), a probe labeling Fe^{2+} or Fe^{3+} (red) and the respective heavy metal ion (blue) were added at 10 μM to the culture sequentially and prior to the addition of the WGA-Alexa Fluor 633 conjugate labeling glycoconjugate (green B. The green shown here is only weakly visible, due to the heavy overlap with red and blue producing a white signal (see color wheel at bottom right). Fe(III) minerals and Fe(III) minerals are visualized by their reflection signal (gray). Brighter colors indicate higher concentrations. The physical dimensions of each image are 17.46×17.46 μm. Scale is the same for all images.
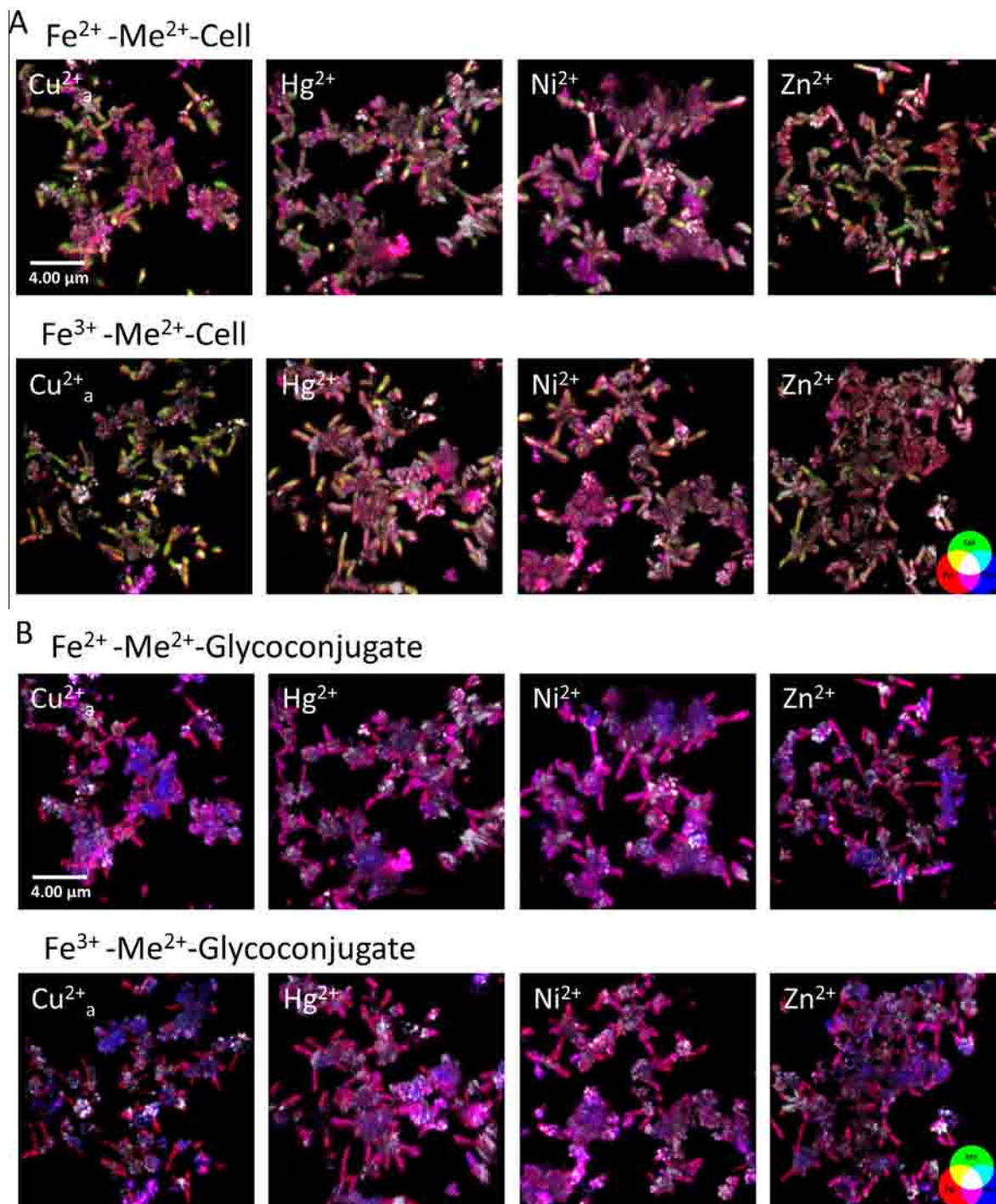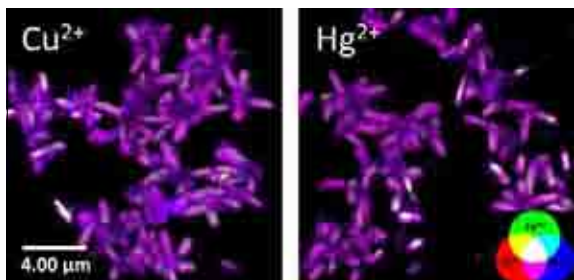
Fig. 3. 2D maximum intensity projections of multiple channels of 3D data sets from CLSM illustrating the sub-μm scale composition of cell-EPS-Fe(III)-minerals aggregates with triple metal ions labeling. Two cultures containing Cu^{2+} and Hg^{2+} were analyzed. Cells were stained with SYTO® 40 blue fluorescent nucleic acid stain (gray), a probe labeling Fe^{2+} (green) and Fe^{3+} (red) and the respective heavy metal ion (blue) added at 10 μM to the culture sequentially. The overlay of all four signals is shown here. The green shown here is only weakly visible, due to the heavy overlap with red and blue producing a white signal (see color wheel at bottom right). Brighter color indicates a higher metal concentrations. The physical dimensions of each image are 17.46 × 17.46 μm. Scale is the same for all images.

the presence of more Fe^{2+} triggered the cells to secrete more glycoconjugates that provided bonding sites for Fe^{3+} complexation and resulted in the formation of aggregates with increased heavy metal sorption (Fig. 4A). The susceptibility of cells to toxic effects was always lower for cell-EPS-Fe (III)-minerals aggregates as compared to phototrophic planktonic cells cultivated chemotrophically under H_2 (Fig. 4B and C). Under Fe(II)-oxidizing conditions, heavy metals, such as Cu^{2+}, Hg^{2+}, Ni^{2+} and Zn^{2+} sorbed to glycoconjugates and minerals, likely lowering the free concentration to less toxic levels. The observed correlation between metal-ion physicochemical properties and planktonic-cell vs. cell-EPS-Fe(III)-minerals aggregates susceptibility to toxic effects indicates a systematic interrelation. Furthermore, the results demonstrate that growth in aggregates, where minerals and glycoconjugates are produced (Fig. 4A), may protect the bacteria from toxic effects (Fig. 4B, 4C).

3.2. Quantitative analysis

When the glycoconjugates were removed by enzymatic digestion prior to incubation with the metal species, and after dissolution of the mineral phases, a higher sorption of the respective metal species to the cells' surfaces was observed when compared to samples that contained native glycoconjugates (Fig. 5B). Glycoconjugate removal reduced the total amount of sorbed heavy metals (Fig. 5A). In contrast, the removal of minerals resulted in larger total amounts of heavy metal sorption to glycoconjugates and cell surfaces (Fig. 5A, B). In triple metal labeling image, lower Fe^{2+} concentrations but higher Fe^{3+} concentrations associated with the glycoconjugates were also observed (Fig. 5C), in comparison to higher Fe^{2+} concentrations but lower Fe^{3+} concentrations at the cells' surfaces (Fig. 5D, H).

The heavy metal distribution in the glycoconjugates in the present study with individual, single metal species was heterogeneous both in the original samples and the samples where the minerals had been dissolved, while the distribution on the cell surfaces of these samples was rather homogeneous (Fig. 5B, F). The distribution of heavy metals on cell surfaces of the samples where the glycoconjugates had been digested was also rather homogeneous. The highest signal of heavy metals was detected associated with glycoconjugates in mineral-digested samples, while the glycoconjugate-digested samples showed the lowest heavy metal signals. Metal sorption to the native glycoconjugates was found to be slightly higher as compared to the metal-binding by glycoconjugate-residues after enzymatic digestion (Fig. 5A). The bacterial cells in all systems showed very similar binding patterns. The heavy metal concentrations on mineral-free cells were the highest, followed by the glycoconjugate-digested cells, and then those of the bacteria in undigested samples (Fig. 5B).

In experiments with Fe^{2+}/Fe^{3+} and heavy metals, a heterogeneous distribution of Fe^{2+} and Fe^{3+} both on the cell surfaces and in the glycoconjugates was observed, whereas the heavy metals such as Cu^{2+}, Hg^{2+}, Ni^{2+} and Zn^{2+} were distributed homogeneously on the cells' surfaces, but heterogeneously within the glycoconjugates (Fig. 2). Furthermore, an influence of the higher Fe^{3+} and lower Fe^{2+} concentrations on the distribution of Cu^{2+}, Hg^{2+}, Ni^{2+} and Zn^{2+} within the glycoconjugates was also observed (Fig. 5E, G). Higher Fe^{3+} concentrations coincided with higher metal concentrations, while lower Fe^{2+} concentrations coincided with lower metal concentrations in glycoconjugates, respectively. Relatively high Fe^{2+} concentrations, moderate Fe^{3+} concentrations and lower heavy metal concentrations such as Cu^{2+} and Hg^{2+} (Figs. 3 and 6H) were observed on bacterial cell surfaces in triple metal labeling experiments.

3.3. Co-localization analysis of heavy metals with cell surface, glycoconjugates and iron minerals

Co-localization analysis was used to identify the preferential locations of heavy metal binding. The Pearson's correlation coefficient was calculated to quantitatively describe colocalization of individual metal species and the organic constituents of the cell-EPS-Fe(III)-minerals aggregates (Figs. 6 and 7). For original samples, the degree of co-localization of Cd^{2+}, Fe^{2+} and Pd^{2+} with both cells and glycoconjugates, of Cr^{3+}, CrO_4^{2-}, Hg^{2+}, TBT and Zn^{2+} with glycoconjugates, and of Au^{3+}, Cu^{2+}, Fe^{3+} and Ni^{2+} with cells were within the range from 0.49 to 0.84, indicating strong co-localizations. For glycoconjugate-digested samples, the degree of co-localization of Cd^{2+}, Cr^{3+}, Fe^{2+} and Pd^{2+} with both cells and glycoconjugates, of CrO_4^{2-} and TBT with glycoconjugates, and of Au^{3+}, Cu^{2+}, Fe^{3+} Hg^{2+}, Ni^{2+} and Zn^{2+} with cells were within the range from 0.49 to 0.84, also indicating strong co-localization. For mineral free samples, the degree of co-localization of Au^{3+}, Cu^{2+}, Fe^{2+}, Fe^{3+} and Pd^{2+} with both cells and glycoconjugates, of Cd^{2+}, Cr^{3+}, CrO_4^{2-}, Hg^{2+}, TBT and Zn^{2+} with glycoconjugates, and of Ni^{2+} with cells were within the range
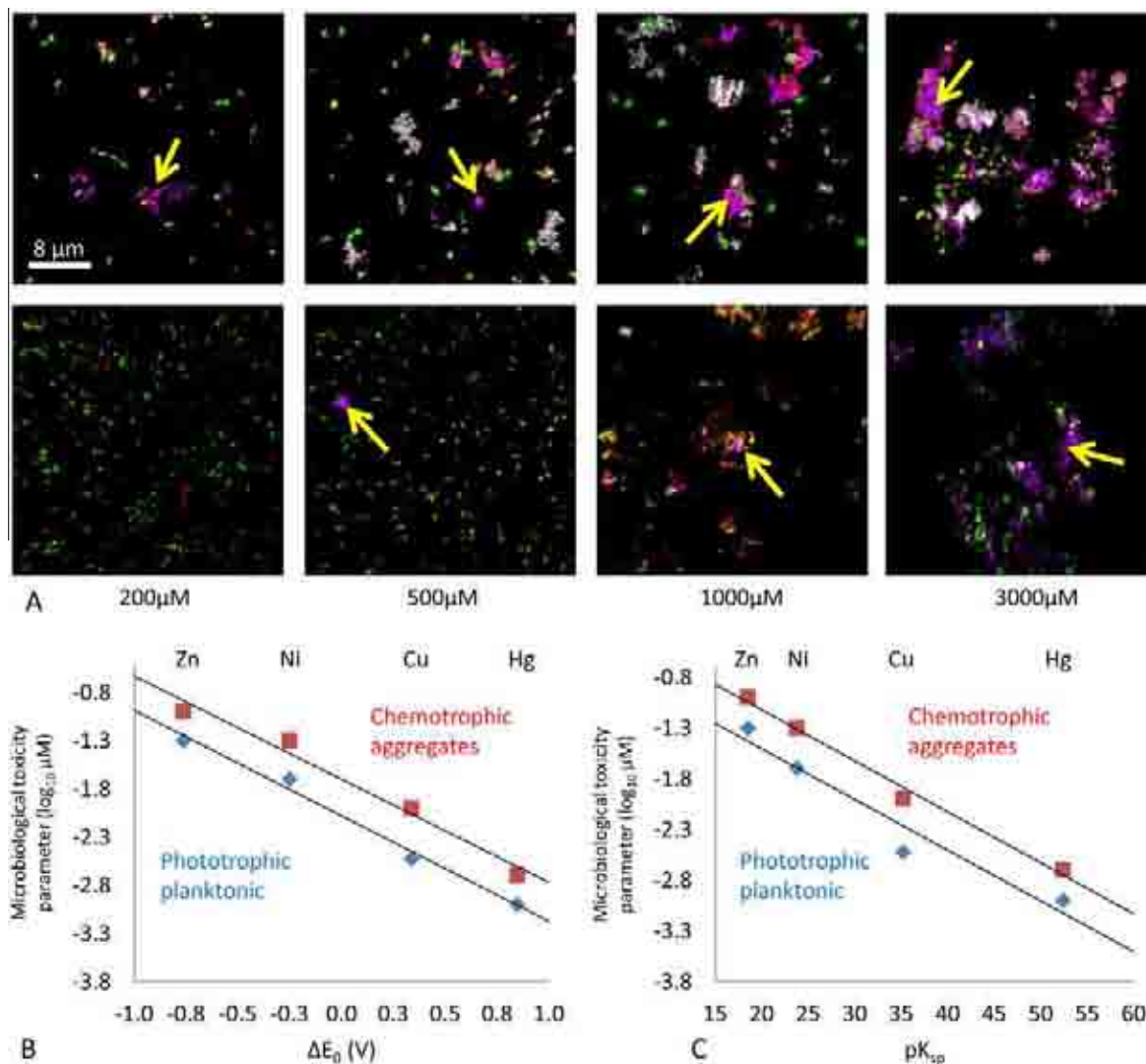
Fig. 4. (A) The oxidation of Fe(II) to Fe(III) by the phototrophic Fe(II)-oxidizing bacterium *Rhodobacter ferrooxidans* strain SW2 triggers the secretion of glycoconjugates, as well the accumulation of Fe(III) minerals, which in combination form cell-EPS-Fe(III)-minerals aggregates (A top row). In contrast, when grown with H_2 as electron donor (A bottom row), less or no formation of aggregates was observed. Cells were stained with SYTO® 9 green fluorescent nucleic acid stain (green), a probe labeling Fe^{3+} (red) and the WGA-Alexa Fluor 633 conjugate labeling glycoconjugates (blue). The arrows indicate examples of the observed increase of EPS and aggregate size with increasing Fe^{2+} concentrations. This was also confirmed independently by larger scale (100 s of μm) CLSM mapping followed by quantitative analysis. Initial Fe^{2+} concentrations are indicated below the images. (B) Correlation between metal-ion physicochemical properties and planktonic-cell vs. cell-EPS-Fe(III)-minerals aggregates susceptibility to toxic effects (the microbiological toxicity parameter describes the upper limit of the concentration range wherein no toxic effects are observed, i.e. the minimum inhibitory concentration). Chemotrophic aggregates (grow on Fe^{2+}, red) and phototrophic planktonic-cell (grow on H_2, blue) susceptibility data plotted against standard reduction potential (ΔE_0) (B) and the (pK_{SP}) (C). These correlations lead to the hypothesis that growth in aggregate with more EPS production might protect the bacteria from toxic effects caused by the metal species. Scale is the same for all images.

from 0.49 to 0.84, also indicating strong co-localization (Fig. 6). The degree of co-localization of Au^{3+}, Cu^{2+}, Fe^{3+} and Ni^{2+} with cells and glycoconjugates seems to be dominated by the cells surfaces in comparison to the glycoconjugates, as shown by the higher coefficients, whereas the degree of co-localization of Cd^{2+}, Cr^{3+}, CrO_4^{2-}, Hg^{2+}, TBT and Pd^{2+} with cells and glycoconjugates was found to be dominated rather by the glycoconjugates. The degree of

co-localization of Fe^{2+} and Zn^{2+} was similar for cells and glycoconjugates. However, the degrees of co-localization of cells with glycoconjugates and of heavy metal with mineral residues in these samples ranged from 0.1 to 0.49, indicating moderate colocalizations (data not shown).

In experiments with two metal species, the degree of co-localization of Cu^{2+}, Hg^{2+}, Ni^{2+} and Zn^{2+} with glycoconjugates and cells were in the range around 0.49
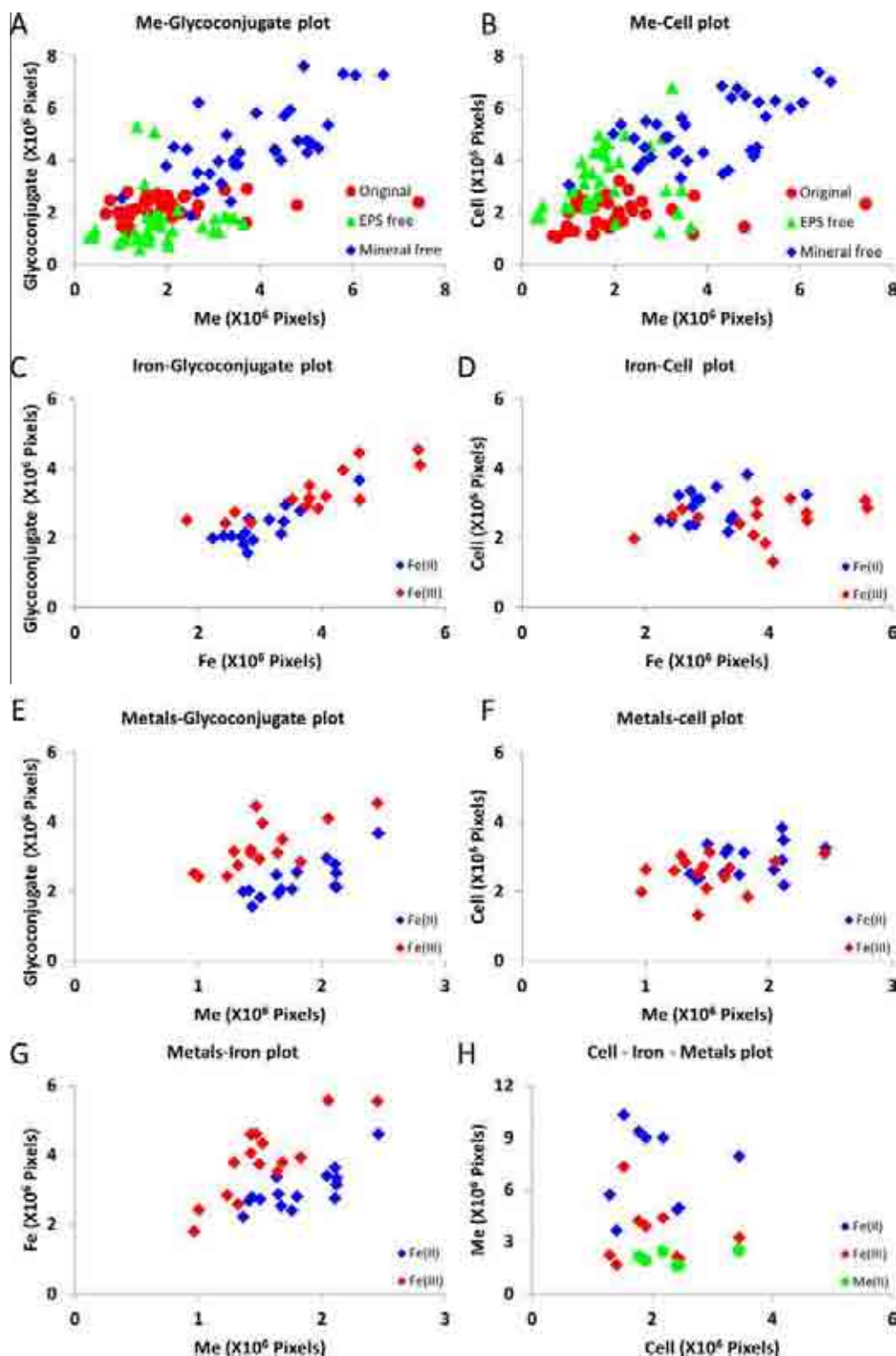
Fig. 5. Relationship between fluorescent intensity of heavy metals, cells, and glycoconjugates in the cell-EPS-Fe(III)-minerals aggregates as calculated by JImageAnalyzer. The plotted value represents the volume wherein the chemical species was detected with intensities above a certain fluorescence intensity threshold. The native glycoconjugates and the bacterial cell surfaces show a similar heavy metal sorption behavior; the removal α-1,4-glucosidic bonds within glycoconjugates reduces its binding sites for all the heavy metals but increase the binding sites on bacterial cell surfaces; in contrast, mineral removal releases more binding sites both in the glycoconjugates and at bacterial cell surfaces (A and B, data from Fig. 1). Glycoconjugates are associated with higher Fe^{3+} and lower Fe^{2+} values, whereas bacterial cells are associated with higher Fe^{2+} and lower Fe^{3+} values (C and D, data from Fig. 2). The values of metals within glycoconjugates depend on Fe^{2+} and Fe^{3+} values (E and F, data from Fig. 2) but their counterpart on the cells' surfaces show similar values (F, data from Fig. 2). Bacterial cell surfaces show higher Fe^{2+} values, lower Fe^{3+} values and lowest metal values (H, data from Fig. 3).
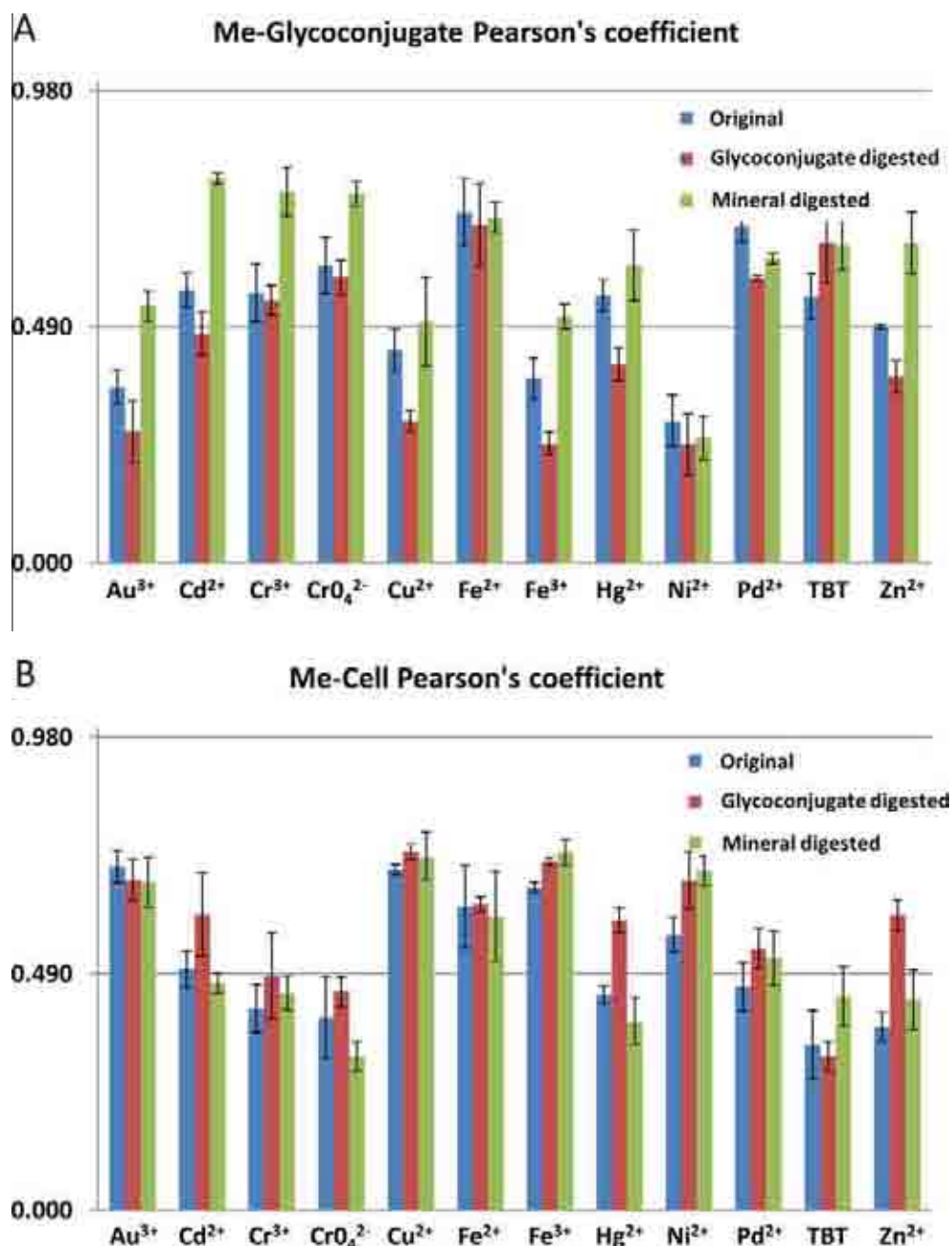
Fig. 6. Quantitative analysis of the colocalization of heavy metals with bacterial cell and glycoconjugates in Fig. 2. Comparison of Pearson's correlation coefficient obtained from 3D-datasets of cell-EPS-Fe(III)-minerals aggregates stained for heavy metals and glycoconjugates (A), heavy metals and bacterial cells (B). All coefficients were calculated without background subtraction. Bio-essential metals (Cu^{2+} and Ni^{2+}) show different colocalization patterns as compared to toxic metals (Cd^{2+}, Cr^{3+}, CrO_4^{2-}, Cu^{2+}, Hg^{2+}, Pd^{2+} and TBT). Glycoconjugate digestion leads to decreasing metal co-localization with glycoconjugates (A red) and increasing the metal co-localization with cells (B red). Mineral digestion increases metal co-localization with glycoconjugates and cells (A and B green). Error bars indicate standard deviations (2σ). (For interpretation of the references to color in this figure legend, the reader is referred to the web version of this article.)

(Fig. 7A, B); the degree of co-localization of Fe^{2+} with glycoconjugates was in the range between 0.49 and 0.84, indicating strong association, whereas Fe^{3+} and glycoconjugates showed only moderate co-localization(Fig. 7D). Cells and heavy metals showed high co-localization with Fe^{2+} and Fe^{3+} compared to the minerals (Fig. 7C, E), which only showed moderate Fe^{2+} and Fe^{3+} co-localization. Cu^{2+},

Hg^{2+}, Ni^{2+} and Zn^{2+} co-localization with Fe^{2+} and Fe^{3+} were between 0.49 and 0.84, indicating strong association with the exception of Cu^{2+} with Fe^{3+}, which had only weak relative co-localization (Fig. 7C). Based on their co-localization with the Fe-species, all the metals were grouped into two groups: the degree of co-localization of Cu^{2+}, Hg^{2+} and Ni^{2+} with glycoconjugates in the "Fe^{2+} group" showed
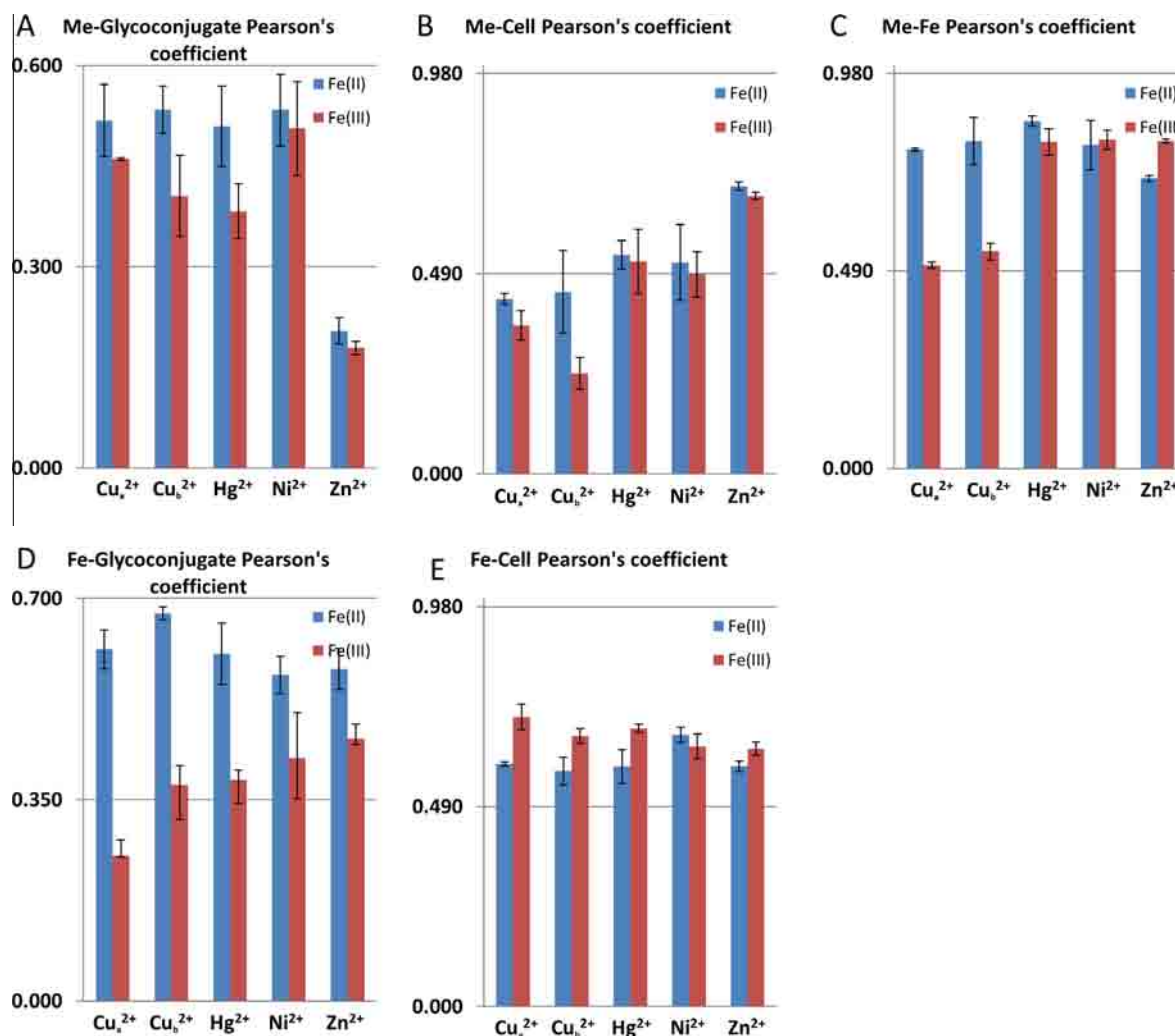
Fig. 7. Quantitative colocalization analysis of heavy metals, Fe^{2+}, and Fe^{3+} with bacterial cells and glycoconjugates, as well as heavy metals with Fe^{2+} and Fe^{3+} in Fig. 3. Comparison of Pearson's correlation coefficients obtained from 3D datasets of cell-EPS-Fe(III)-minerals aggregates stained for heavy metals and glycoconjugates (A), heavy metals and bacterial cells (B), heavy metals and Fe^{2+}/Fe^{3+} (C), Fe^{2+}/Fe^{3+} and glycoconjugates (D), Fe^{2+}/Fe^{3+} and bacterial cells (E); all coefficients were calculated without background correction. Fe^{2+} and Fe^{3+} show a similar degree of colocalization with bacterial cells but different preferences to glycoconjugates; heavy metals are preferentially associated with the glycoconjugates and are colocalized with Fe^{2+} and Fe^{3+}. Error bars indicate standard deviation (2σ).

strong co-localization, while Cu^{2+}, Hg^{2+}, and Ni^{2+} with glycoconjugates in the "Fe^{3+} group" showed moderate co-localization only; Zn^{2+}, however, showed moderate co-localization; the degree of co-localization of Hg^{2+}, Ni^{2+}, and Zn^{2+} with cells showed strong co-localization, while Cu^{2+} showed moderate co-localization with cells; but all metals showed moderate co-localization with glycoconjugate residuals in the samples wherein glycoconjugates were enzymatically digested.

3.4. Correlation analysis of heavy metals with cell surface, glycoconjugates and iron minerals

Correlation analysis was used to further analyze the mechanisms involved in Fe(II) oxidation and heavy metal binding. Scalar numbers such as statistical indicators (e.g. Pearson's coefficients) have the advantage of being easy to

handle, but they only describe certain aspects of the datasets. To provide additional insights into the pairwise relationship of variables, the signals of pairs of images/components were visualized by scatterplots to highlight spatial correlations. The results indicated that Fe^{2+} and Fe^{3+} show similar behavior, as both can be found in association with cells and with glycoconjugates. It appears that a fraction of the detected Fe^{3+} is co-localized with glycoconjugates, as shown by the broad trend of pixels in Fig. 8C. The distributions of Ni^{2+} and Hg^{2+} are similar to each other and distinct from what can be observed for Fe^{2+} and Fe^{3+}. Both show a similar relationship with cells. In both scatterplots, i.e. Ni^{2+}/cell (Fig. 8F) and Hg^{2+}/cell (i.e. cells represented by DNA) (Fig. 8H), one broad trend is visible, indicating the co-localization of part of the detected metals with bacterial cells. However, for both metals the highest concentrations were detected apart from the
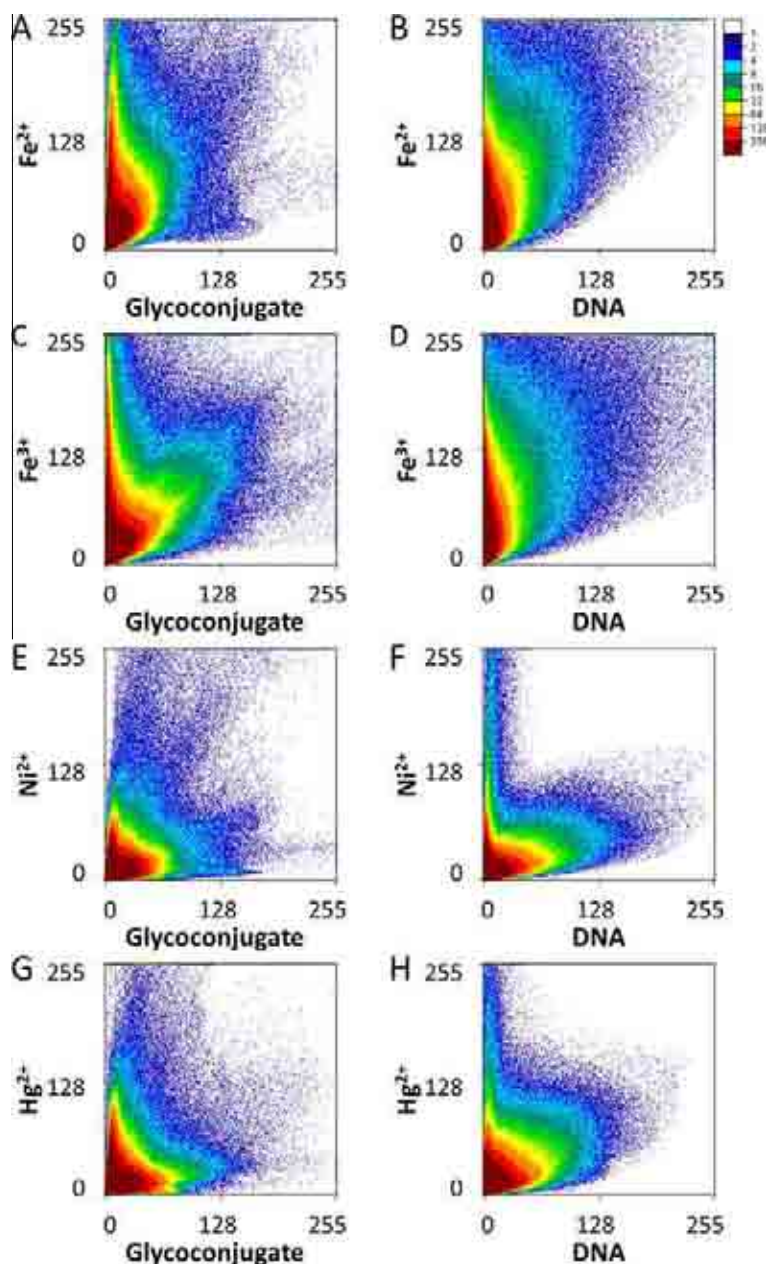
Fig. 8. The scatterplots illustrate the fluorescence intensity of individual pixels for metal ions, and glycoconjugates or cells (DNA). Colors represent the frequency of occurrence of pixels with a certain intensity. Scatterplots are shown for Fe^{2+} (A, B; $Fe^{2+} - Ni_a^{2+}$ in Fig. 3), Fe^{3+} (C, D; $Fe^{3+} - Ni_a^{2+}$ in Fig. 3), Ni^{2+} (E, F; $Fe^{2+} - Ni_a^{2+}$ in Fig. 3) as an example for a bio-essential metal, and Hg^{2+} (G, H; $Fe^{2+} - Hg_a^{2+}$ in Fig. 3) as an example for a non-essential metal. Both Fe^{2+} and Fe^{3+} show similar behavior and are found in association with cells and with glycoconjugates. The distributions of both Ni^{2+} and Hg^{2+} are similar to each other and distinct from Fe^{2+} and Fe^{3+}, which show a similar relationship with cells.

cells. The relationship of Ni^{2+} and Hg^{2+} with glycoconjugates (Fig. 8E, G) is more complex. The $Ni^{2+}/$glycoconjugates scatterplot shows a fan-shaped point cloud, suggesting Ni^{2+} and glycoconjugates had a wide range of concentration ratios. The point cloud in the $Hg^{2+}/$glycoconjugates scatterplot looks similar to $Ni^{2+}/$glycoconjugates, but might be composed of two broad trends representing more distinct high and low $Hg^{2+}/$glycoconjugates ratios respectively. In summary, for both Ni^{2+} and Hg^{2+},

the scatterplots clearly indicate sorption of these metals to bacterial cells and glycoconjugates. While sorption to cells is represented by comparably regular clusters in the scatterplots, the metals were detected in more varying ratios to glycoconjugates.

The hierarchical group approach of heatmaps (Fig. 9), complemented by principal component analysis (PCA, Fig. 10), were used to evaluate the similarity of heavy metals sorption in the cell-EPS-Fe(III)-minerals aggregates.
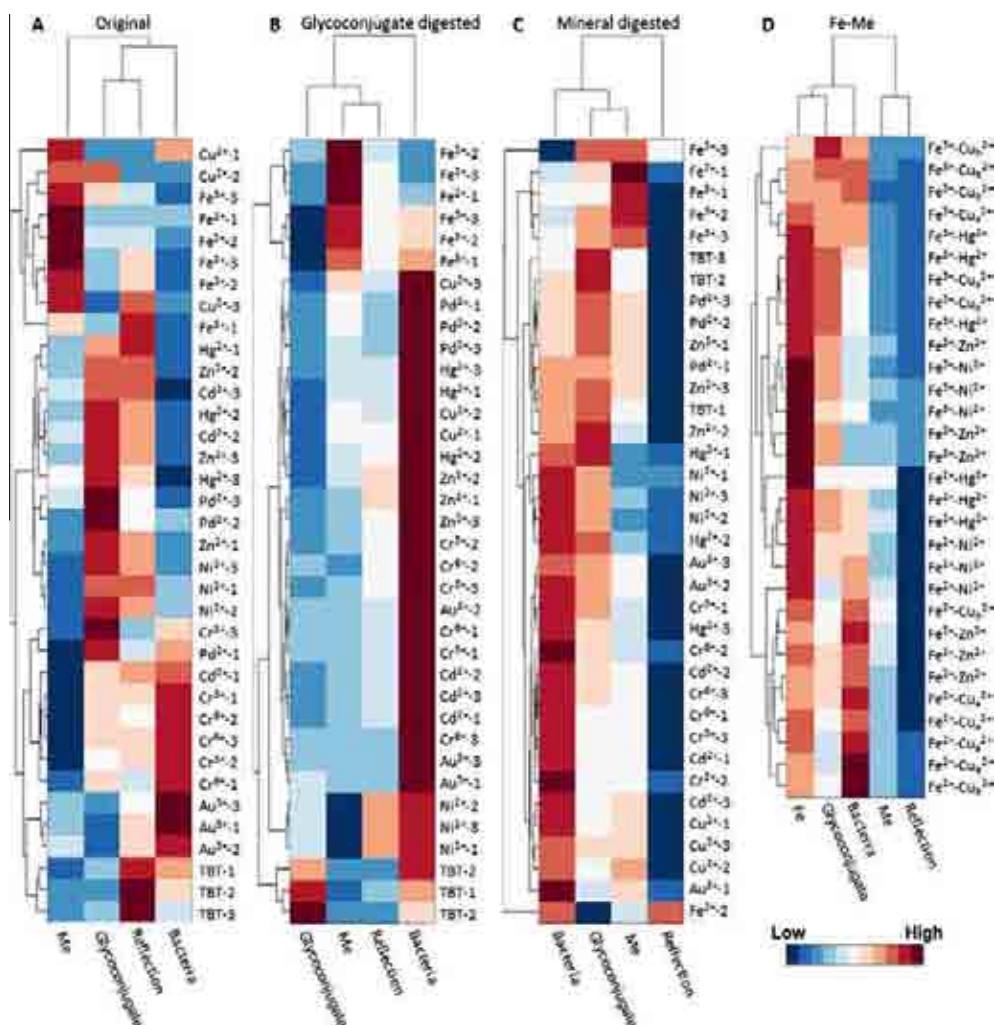
Fig. 9. The heatmaps represent a hierarchical group similarity analysis of the bacterial cells, glycoconjugates and biogenic mineral residuals from 3D stacks using CLSM with sorbed heavy metals. The relative volume of heavy metals (Me), glycoconjugates, bacterial cells (Bacteria) and minerals (Reflection) are indicated by the color of scale. The heatmap reveals that heavy metals show different associations with bacterial cells' surfaces and glycoconjugates in original cell-EPS-Fe(III)-minerals aggregates (A), in systems where α-1,4-glucosidic bonds within glycoconjugates were split by glucoamylase enzymic digestion (B), and in systems where minerals removed by Fe-oxide oxalate digestion (C), and finally for Fe^{2+}/Fe^{3+} and heavy metal dual-labeling of the original cell-EPS-Fe(III)-minerals aggregates (D).

Both approaches do not require any a priori knowledge on grouping, and they consistently showed similarly strong groupings of samples based on their treatments. PCA of the original aggregates showed that principal components 1 and 2 explained 36.43% and 30.87% of the variations, respectively. There were four groups shown in the Fig. 10A, which was also supported by the heatmap analysis (Fig. 9A). The analysis indicated that Zn^{2+} and Ni^{2+} formed a group that has stronger relationships with glycoconjugates; Cd^{2+}, Hg^{2+}, Pd^{2+} and Cu^{2+} have unclear relationships with glycoconjugates and cell surfaces, whereas Fe^{2+} and Fe^{3+} showed stronger correlations with glycoconjugates as compared to cell surfaces. The more toxic heavy metal ions such as Cr^{3+}, CrO_4^{2-} and Au^{3+} formed a separate group associated with the cell surface, while TBT (organotin compound, $(C_4H_9)_3Sn$) behaved differently than all other metals. The PCA of the experiments where glyco-

conjugates were removed showed that principal components 1 explained 53.98% of the variation while principal components 2 explained 24.47% (Fig. 10B). Based on the PCA and heatmap analysis (Fig. 9B), almost all of the metals mapped in this study show very weak correlations with bacterial cell surfaces. Only Fe^{3+} and Fe^{2+} form a separate group, neither associated with glycoconjugates nor cell surfaces (Fig. 10B). In the experiments wherein the minerals were removed from the system, the first two PCA principal components explained 85.96% of the variation, specifically principal components 1 and 2 explained 60.84% and 25.12%, respectively (Fig. 10C). Almost all heavy metals show various correlations with both bacterial cells and glycoconjugates, but Fe^{3+} and Fe^{2+} again form a separate group neither associated with glycoconjugates nor cell surfaces (Figs. 9C, 10C). In dual labeling experiments of Fe^{3+}/Fe^{2+} and the respective heavy metals in the original
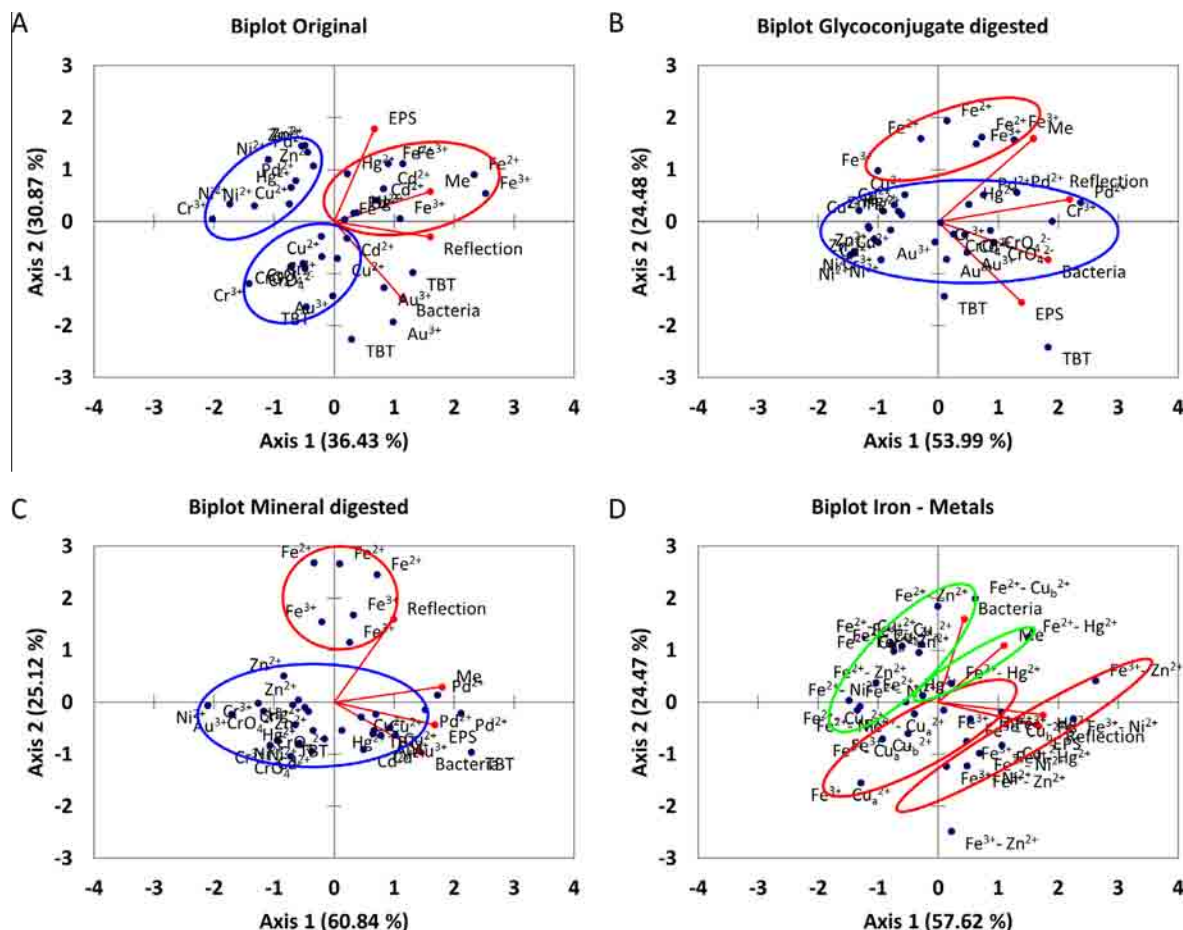
Fig. 10. Biplots of principle components of the volumes occupied by bacterial cells, glycoconjugates and biogenic mineral residuals from 3D stacks using CLSM with sorbed heavy metals. PCA indicates associations between metal species abundances and cells, and between metal species abundances and glycoconjugates. It shows strong grouping based on different treatments. The results of the PCA revealed that heavy metals have various associations with bacterial cells' surfaces and glycoconjugates in the original cell-EPS-Fe(III)-minerals aggregates (A), in systems where α-1,4-glucosidic bonds within glycoconjugates were split by glucoamylase enzymic digestion (B), in systems where minerals removed by Fe-oxide oxalate digestion (C), and in original cell-EPS-Fe(III)-minerals aggregates where Fe^{2+}/Fe^{3+} and heavy metal dual staining was used (D).

samples, the first principal component explained 57.61%, and the second principal component explained 24.47% of the variation (Fig. 10D). It showed that in the dual metal ion labeling, the Fe^{3+} group had a strong association with glycoconjugates, and that the Fe^{2+} group had a strong association with bacterial cells. Cu^{2+}, Ni^{2+}, Zn^{2+} and Hg^{2+} have similar associations with both Fe^{3+} and Fe^{2+} (Figs. 9D, 10D). Thus, dual metal labeling in combination with PCA and heatmap analysis allowed for identifying groups of metals with similar behavior.

3.5. Mineralogical analysis

The dried mineral products of the microbial Fe(II) oxidation in the presence of the different metals were analyzed using μXRD (Fig. 11). Each sample exhibited reflections corresponding to goethite, while samples without the addition of heavy metals, samples $+Ni^{2+}$, and samples $+Hg^{2+}$ had some additional reflections corresponding to siderite.
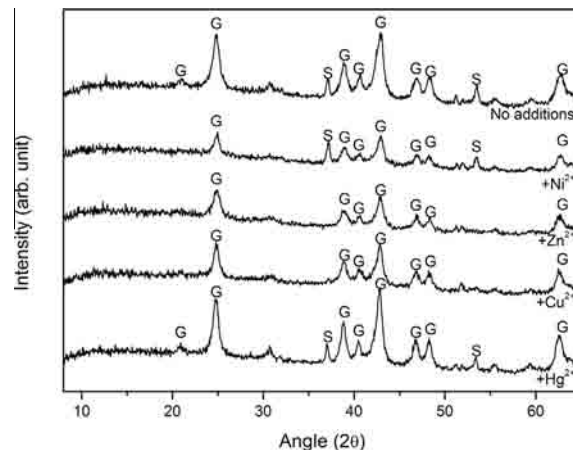

Fig. 11. Micro X-ray diffraction (μXRD) dried mineral phases formed in the presence of no additions, $+Ni^{2+}$, $+Zn^{2+}$, $+Cu^{2+}$ and $+Hg^{2+}$. Reflections correspond to goethite (G) and siderite (S).
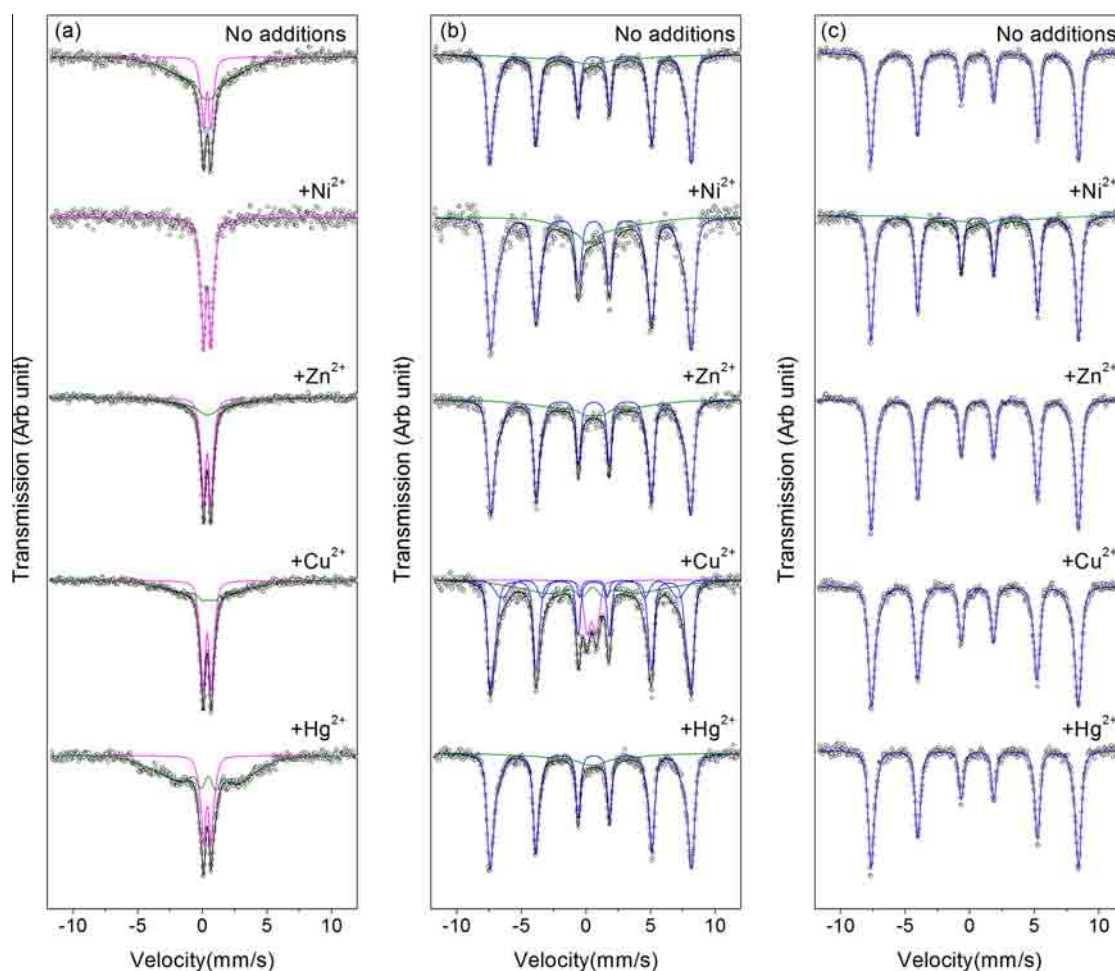
Fig. 12. Mössbauer spectra of solid mineral phases formed in the absence of additions or with addition of Ni^{2+}, Zn^{2+}, Cu^{2+}, Hg^{2+} with spectra collected at (a) 295 K, (b) 77 K and (c) 4.2 K. Data points are shown as open circles, with individually fitted components corresponding to paramagnetic doublets (magenta), paramagnetic goethite (green), magnetically ordered goethite (blue). (For interpretation of the references to color in this figure legend, the reader is referred to the web version of this article.)

The broad linewidth observed for the goethite reflections suggests poor mineral crystallinity, or small average particle size.

^{57}Fe Mössbauer spectroscopy (Fig. 12, Table S1) was carried out at three different temperatures (295 K, 77 K and 4.2 K) with the final mineral products after complete Fe(II) oxidation in order to determine if metal substitution induced changes to the mineralogy of the Fe oxyhydroxides that were produced. It is clear from examination of the room temperature spectra (295 K) that all samples are dominated by a doublet (Db) combined with a collapsed sextet (para Gt.), except for the sample amended with Ni^{2+} for which no collapsed sextet is present (Fig. 12a). The hyperfine parameters of the doublets are approximately equal for all samples, with center shift (CS) of 0.36–0.37 mm/s and quadrupole splitting (QS) of 0.65–0.71 mm/s. These parameters are indicative of octahedrally coordinated Fe (III) (Murad, 2010). Based on the room temperature measurements alone, it is not possible to identify the mineral phase; however, the presence of collapsed sextets indicates

partial magnetic ordering. The collapsed sextets have more varied CS and QS values, but show similar hyperfine fields (H; 15–21 T). The relative proportion of the collapsed sextets varies for all samples ranging from just 37% in the sample amended with Zn^{2+} to 71% in the sample without metal amendments.

At 77 K, the spectra are almost completely magnetically ordered (Fig. 12b). All samples except for $+Cu^{2+}$ are dominated by an ordered sextet, which displays the hyperfine parameters of goethite at 77 K, with CS $\sim$ 0.48 mm/s, QS $\sim$ 0.24 mm/s and H $\sim$ 47 T. Samples also required an additional collapsed sextet (para. Gt), indicating that samples were not fully magnetically ordered. The sample amended with Cu^{2+} required the presence of an additional doublet to accurately fit the data. The doublet accounted for 10% of the relative area and had CS and QS values of an octahedrally coordinated Fe(III) mineral that was likely superparamagnetic goethite. Spectra recorded at 4.2 K show complete magnetic ordering except for the sample containing Ni^{2+}, which required the use of a collapsed

sextet (13% relative area) in order to obtain the best fit (Fig. 12c). The ordered sextets showed very similar parameters in all samples with CS ranging from 0.48 to 0.49 mm/s, QS from -0.20 to -0.22 mm/s and H from 49.0 to 49.5 T.

4. DISCUSSION

4.1. Advantages of CLSM in combination with fluorescence labeling – Spatially resolved analytics vs. conventional approaches

CLSM in combination with metal-sensitive fluorescence labeling and probes specific for DNA or polysaccharides was chosen as a very promising approach for studying the binding of heavy metals to aggregates of bacteria, microbially produced EPS, and microbially precipitated Fe(III) minerals. This approach, based on the 3D visualization of the Fe^{2+}/Fe^{3+} and heavy metal distributions in cell-EPS-Fe(III)-minerals aggregates, allows for samples to be analyzed in their natural, hydrated state. Thus, the measured distribution of the relevant chemical species are not affected by artifacts from sample preparation such as freeze-drying or CPD that is necessary for electron microscopy (EM) based analytics. These sample preparation approaches for EM often cause EPS loss or dehydration and collapse, integrity loss and cellular shrinkage (Dohnalkova et al., 2011).

Our CLSM based approach allows for quantification of the inherent heterogeneity of aggregates, as well as correlations of certain chemical species with the goal of identifying sorption mechanisms. Additionally, the approach of this study is complementary to existing technologies for exploring 3D *in-situ* bacterial microenvironments (Wessel et al., 2013). It might be also a powerful tool to study the sorption and fate of iron and trace metals in the environments (Morel and Price, 2003; Boyd and Ellwood, 2010). This is an important step towards a detailed understanding of spatial microscale processes and mechanisms of metal binding in complex heterogeneous systems such as cell-EPS-Fe(III)-mineral aggregates, which are usually not possible using conventional approaches such as sequential extractions of metals from bulk samples, which sometimes contradict model estimations (Cui and Weng, 2015). In contrast to these bulk approaches, the present study captures the 3D heterogeneity of such systems, providing evidence of the contributions of organic and mineralogical phases to the sorption of metal species.

4.2. Optimization of the CLSM approach

4.2.1. Data acquisition

For CLSM mapping, it is essential to select appropriate metal fluorescent probes. Thus, the selection requires a careful considerations of their limitations. Currently there are only few well-established but rather poorly selective metal fluorescent probes such as Fura-2, Newport Green and Fluozin-1 available for labeling Ni^{2+}, Zn^{2+}, and Cd^{2+}. As a result, only a very limited number of studies

have shown heterogeneous metal distributions in biofilms (McCall and Fierke, 2000; Wuertz et al., 2000; Ueshima et al., 2008). So far only one ferric chemosensor has been reported for imaging ferric iron distribution in oral biofilms by CLSM using microfluidic devices (Shumi et al., 2010). Although various metal fluorescent probes and their applications have been summarized in a recent review (Carter et al., 2014), most of the probes have been developed for detecting intracellular metal concentrations. In an earlier study we have developed guideline (Hao et al., 2013) for selecting probes for environmental applications. One essential parameter for an appropriate selection is the concentration range of the respective target metal ion. For most bacteria, for example, intracellular total metal concentrations are in the range of 10^{-2} M for K and Mg, around 10^{-4} M for Ca, Zn, and Fe, 10^{-5} M for Cu, Mn, Mo and no more than 10^{-6} M for V, Co, and Ni (Finney and O'Halloran, 2003).

Another important parameter to be considered is the stability of the complex of the metal fluorescent probes with the target ions in comparison to the organic ligands present in the sample. In a 1:1 stoichiometry, most dissociation constants (K_d) for metal ions, such as Fe^{3+} (Witter et al., 2000), Fe^{2+} (Ba et al., 2009), Cu^{2+}, Ni^{2+}, Zn^{2+} (McCall and Fierke, 2000), Pb^{2+}, Cd^{2+}, (Comte et al., 2006, 2008) and Hg^{2+} (Ravichandran, 2004) with organic ligands are in the 10^{-6} to 10^{-5} range. While the K_d of metal ions with goethite (Cu^{2+}, Cd^{2+}, Zn^{2+}, Pb^{2+}, Co^{2+}, Ni^{2+} and Cr^{3+}) and ferrihydrite (Cd^{2+}, Zn^{2+} and Co^{2+}) are in the range of 10^{-2} to 10^1 and 10 to 10^3, the K_d of Hg^{2+} with goethite and ferrihydrite are in the range of 10^{-4} and 10^{-7}, respectively (Dzombak and Morel, 1990; Appelo and Postma, 2005; Fischer et al., 2007; Karamalidis and Dzombak, 2011). The ranges of metal concentrations that can be sensed by metal fluorescent probes are determined by the K_d values (Penner-Hahn, 2013). Most metal probes were designed to change their emitted fluorescence intensity in response to Me^{n+} at a concentration range between $0.1 \times K_d$ to $10 \times K_d$ (Takahashi et al., 1999). For the probes to be applicable for environmental research, such as metal mapping in cell-EPS-Fe(III)-minerals aggregates or biofilms as is carried out here, it is necessary to select groups of metal fluorescent probes with appropriate ranges of K_d values.

4.2.2. Data analysis

Another aspect of optimization of this approach is the required data analysis. For the analysis of spatially resolved, microscopic data, approaches such as correlation analysis in scatterplots (e.g. with the ImageJ plugin ScatterJ (Zeitvogel et al., 2014)) or quantitative co-localization analysis are always limited to two-component relationships. Comprehensive software packages (e.g. Imaris; Zurich, Switzerland) and automated thresholding algorithms (Costes et al., 2004) facilitate an efficient 3D colocalization analysis. The degree of colocalization can be used to describe associations of the heavy metals with bacterial cell surfaces and glycoconjugates (Jaskolski et al., 2005; Malkusch et al., 2012). Additionally, principal component

analysis (PCA) can be used on the data. In the present study, we used JImageAnalyzer to identify interrelations between heavy metal species' abundances, and bacteria or glycoconjugates that were not apparent using the previously described simple pair-wise analysis. This multivariate statistical analysis facilitates the visualization of grouping as well as displaying variances and correlations by creating two-dimensional biplots of the principle components (Gabriel, 1971).

4.3. Significant influence of bacterial cells' surfaces and EPS on heavy metal sorption

Enzymatic digestion of the glycoconjugates reduces the amount of available binding sites while (Fig. 5A) Fe(III) oxyhydroxide dissolution exposes more binding sites of the glycoconjugates and of the bacterial cells' surfaces (Fig. 5A, B), although both approaches destroyed the integrity of cell-iron-EPS-mineral aggregates and resulted in changes of Fe^{3+} and Fe^{2+} *in-situ* distribution (Fig. 10B, C). These results indicate that bacterial cells are responsible for the majority of the sorption of certain metal species in cell-EPS-Fe(III)-minerals aggregates (e.g. bacterial cells sorbed 67% of Cu^{2+}, S2). Thus, the results of the present study are in general agreement with previous studies on sorption of heavy metals such as Hg^{2+} (65%) (Fein et al., 2001), Cd^{2+} (80–90%), Zn^{2+} (80–90%) (Plette et al., 1996; Späth et al., 1998) Ni^{2+} (67%), Co^{2+} (72%), Cu^{2+} (76–90%), Pb^{2+} (90%) (Daughney et al., 1998; Choudhary and Sar, 2009) and CrO_4^{2-} (50–100%) (Srinath et al., 2002; Goyal et al., 2003; Loukidou et al., 2004) that preferentially bind to bacterial cells over glycoconjugates. The results of the present study are also in agreement with two studies wherein nearly all Fe^{3+} was sorbed to bacterial cell surfaces and the biofilm matrix (Daughney et al., 2001; Julien et al., 2014). However all these studies only considered cells and potentially some EPS associated with the cells, but not Fe(III) minerals as in the present study. In summary, the current study verifies that bacterial cell surfaces have the potential for sorption of large quantities of heavy metals (Ag^+ Cu^{2+} Ni^{2+} Cd^{2+} Pb^{2+} Zn^{2+} Cr^{3+}) (Mullen et al., 1989; Geesey et al., 2008).

Other studies have reported that EPS can complex Co^{2+} (69%), Ni^{2+} (37%) (van Hullebusch et al., 2005), Cu^{2+} (54%) and Cd^{2+} (9%) (Sterritt and Lester, 1980), and that pure synthetic goethite can also complex Zn^{2+} (69%), Cr^{3+} (67%), Pb^{2+} (54%), Cd^{2+} (50%) and Ni^{2+} (50%) (Francis and Dodge, 1990). In the present study, the amounts of heavy metals sorbed by the organic constituents of the cell-EPS-Fe(III)-minerals aggregates and biofilms are reduced by the sorption of Fe^{2+}, Fe^{3+} and Fe(III) minerals, and thus reduce the amount of sorption sites available for adsorption of other metals, a process that has previously been described (Daughney et al., 2011). In the present study, glycoconjugates sorbed 20% of Cu^{2+}, while minerals were responsible for approximately 13% (Fig. S2). This in general confirmed the previous reports that EPS contributes to sorption of 14% of Ni^{2+} in aerobic granules (Liu and Xu, 2007), and that minerals account for 12% of Cd^{2+}, Pb^{2+},

Ni^{2+} and iron (Guibaud et al., 2005; Julien et al., 2014) in activated sludges and biofilm.

The binding of metals in cell-EPS-Fe(III)-minerals aggregates analyzed in the present study is in agreement with various earlier studies and can be summarized as, (1) the organochemical composition of glycoconjugates determines the total number of binding sites (cf. Guibaud et al., 2003; More et al., 2014); (2) Fe^{2+}, Fe^{3+} and Fe(III) minerals bind to the glycoconjugates in large amounts and thus, determine the fraction of binding sites that remain available for additional other heavy metals; (3) the characteristics of the functional groups on the cell surfaces and within the glycoconjugates, and in particular their affinity and specificity for certain metal species and their respective concentration determine the fractions of heavy metal species bound in the system (cf. Kulczycki et al., 2002; Fang et al., 2009).

Eickhoff and coworkers have shown that in systems that contain biogenic ferrihydrite, microbial cells and EPS, Ni^{2+} is preferentially bound to the ferrihydrite and competes with the organic molecules for sorption sites (Eickhoff et al., 2014). In contrast, it has also been reported that minerals associated with microbial EPS contain more trace metals as compared to abiotic mineral phases (d'Abzac et al., 2013), and therefore might reduce heavy metal sorption to bacterial cells (Teitzel and Parsek, 2003; Waychunas et al., 2005), and act as a protective barrier (Comte et al., 2006). Finally, in such systems, metals with small ionic radii (e.g., Co^{2+} and Cd^{2+}) can be incorporated into the Fe(III) oxide crystal structure (Lack et al., 2002), but results in the present study suggest that there has been no significant substitution of any metals into the goethite mineral structure. Whereas one could argue that this maybe due to the fact that heavy metals bound to mineral surfaces are not readily labeled by the approach used here (Hao et al., 2013), the labeling results are in keeping with the results of Moessbauer spectroscopy that did not indicate an incorporation of major amounts metals into the crystal structure as discussed in detail later.

The similar sorbent properties of cell surfaces and glycoconjugates observed in this study (Fig. 7A, B) indicate that both organic phases host similar concentrations of metal sorption sites with similar binding mechanisms for the different metals. The results of this study are consistent with those of previous studies on *Bacillus subtilis* and *Pseudomonas putida* (Ueshima et al., 2008; Fang et al., 2014). Three main mechanisms have been claimed to be responsible for the sorption of heavy metal ions to cell surfaces and EPS: First, the sorption of metal cations to deprotonated carboxyl groups and phosphoryl groups that are the dominant binding sites for metals at high metal loadings (Fein et al., 2001; Kulczycki et al., 2002; Fang et al., 2014), while sulfhydryl groups dominate at lower metal loadings (Mishra et al., 2010). These functional groups are deprotonated and are usually negatively charged at neutral pH (Templeton and Knowles, 2009). The second mechanism is the binding of ligands with oxygen as the donor atom to carboxylate, carbonyl, alcohol and phosphoryl groups (Nieboer and Richardson, 1980). Finally, some toxic metal species such as Hg^{2+} Pb^{2+} can be irreversibly bound to

nitrogen and sulfur centers. Many metal species such as Fe^{2+}, Fe^{3+}, Zn^{2+}, Ni^{2+}, Cu^{2+}, Co^{2+}, Mn^{2+}, Cr^{3+} can be bound by all above mentioned mechanisms (Nieboer and Richardson, 1980). Specifically, oxygen-containing functional groups can form complexes with Cr^{3+} (Hong et al., 2012). Bacterial surfaces, however, are dominated by carboxyl and phosphoryl functional groups, which are involved in the sorption of both Fe^{2+} and Fe^{3+} (Gupta et al., 2000; Hegler et al., 2010), most of bioessential metals such like Cu^{2+} (Pokrovsky et al., 2008), Zn^{2+} (Toner et al., 2005; Guine et al., 2006), Ni^{2+} (Sar et al., 2001; Zhu et al., 2010) .

4.4. Ferrous iron induces EPS excretion and cell-iron-mineral aggregation

The results of this present study clearly showed that heavy metal ions, in particular Fe^{2+}, have a strong effect on the excretion of EPS by the bacteria (Fig. 4) and, likely as a result, on the formation of cell-EPS-Fe(III)-minerals aggregates. The effect of Fe^{2+} ions on EPS formation was more obvious than for other metal ions tested. This might be due to the fact that these Fe(II)-oxidizing phototrophic bacteria require high Fe^{2+} concentrations. EPS can enrich bioavailable Fe^{2+} from the surrounding aqueous microenvironment for bacteria to oxidize, with the resulting Fe^{3+} then sorbed or complexed by the EPS, which templates (nano-) crystalline Fe(III) minerals accumulation (Chan et al., 2004; Plach et al., 2011; Elliott et al., 2012; Wu et al., 2014). This series of events may both diminish the concentration of free Fe^{2+}, which is toxic to phototrophic Fe(II)-oxidizing bacteria (Bird et al., 2013), and help to prevent encrustation of the cell with Fe(III) (oxyhdr)oxides (Schädler et al., 2009; Wu et al., 2014), which would prevent diffusion of metabolites. This confirms previous studies, which showed that Fe^{3+} concentrations exceeding levels that induce growth limitation suppresses biofilm formation, whereas Fe^{3+} concentrations that induced growth limitation were essential for the formation of heterotrophic bacterial biofilms (Singh et al., 2002; Banin et al., 2005; Wang et al., 2011). Other studies showed that adding 1 μM Fe^{3+} in the culture medium can promote the production of EPS by biofilms (Jin and Guan, 2014), and both Fe^{3+} and Fe^{2+} alter the amounts of EPS production (Lu et al., 2005; Klueglein and Kappler, 2013). However, when the concentration of heavy metal species exceeded certain threshold values, the effects on the promotion of EPS production became less significant (Sheng and Yu, 2006).

Two main mechanisms that influence the excretion of EPS are involved in the response of microbes to metal concentrations in their aqueous environment. These include sorption to EPS when concentrations of essential metals are low in order to facilitate the uptake of the respective metal species by the cells (Li and Yu, 2014; Tourney and Ngwenya, 2014), or excretion of EPS when toxic metal species concentrations are high. The latter creates a protective envelope with reduced metal concentrations that prevents the uptake of toxic metal concentrations (Valls and de Lorenzo, 2002; Li and Yu, 2014; Tourney and Ngwenya, 2014).

4.5. Influence of Fe(II) oxidation on EPS, aggregation and on heavy metals sorption

In the present experiments, glycoconjugates were not only involved in passive Fe^{2+} enrichment and active Fe^{3+} sorprion, but also in an aggregation of amorphous and poorly crystalline Fe(III) minerals. The precipitation of such mineral phases is caused by the low solubility of Fe^{3+} and rapid precipitation at circumneutral pH (Faraldo-Gomez and Sansom, 2003). Furthermore, the presence of the EPS might prevent the precipitation of or transformation to more crystalline mineral phases (Larese-Casanova et al., 2010; Mikutta et al., 2012). EPS therefore can change the surface properties of the minerals, and the presence of minerals can alter capacity of the EPS for heavy metal sorption (Mikutta et al., 2012). Thereby, the results of the present study are consistent with those of previous studies showing that EPS act as templates for the precipitation of amorphous and (nano-)crystalline Fe (III) minerals (Chan et al., 2004; Plach et al., 2011; Elliott et al., 2012), yet enable microbes to adjust their geochemical microenvironments (Elliott et al., 2014) to enhance microbial growth.

According to our current interpretation, the strain *Rhodobacter* SW2 excretes EPS to enhance Fe^{2+}-binding and thus availability of the electron donor. Subsequently, microbial Fe(II) oxidation results in the release of Fe^{3+} that accumulates in the EPS (Kappler and Newman, 2004; Posth et al., 2014; Wu et al., 2014). EPS and (nano-) crystalline Fe(III) minerals were responsible for the aggregation of cells, EPS and Fe(III) minerals. Therefore, the results of the present CLSM *in situ* analysis at the microscale show that bacterial Fe(II) oxidation is an important process in determining the spatial distribution of iron oxides and the distribution of heavy metals in aqueous environments (Warren and Ferris, 1998).

4.6. Influence of heavy metals on biogenic minerals

Mineralogical analyses provide additional and complementary information of the long-term fate of metals in these systems as the metals are shown not to be incorporated into the stable mineral structure. μXRD and Mössbauer spectroscopy results showed that goethite is the dominant mineral phase that is produced by microbial Fe (II) oxidation by SW2. Previous analyses of the mineral products of SW2 in the absence and presence of Ni^{2+} have indicated that ferrihydrite rather than goethite is the dominant mineral phase, which is produced (Kappler and Newman, 2004; Eickhoff et al., 2014). Differences in the mineral product between the present study and previous work are likely due to an 180 days aging process of the ferrihydrite in batch cultures. During this time, any residual Fe^{2+} could have reacted with the ferrihydrite leading to a transformation to goethite over time (Hansel et al., 2005), or alternatively the transformation could have taken place due to the presence of bicarbonate or drying (Wu et al., 2014; Swanner et al., 2015).

It is known that in room temperature Mössbauer spectra goethite will commonly be visible as magnetically split

spectra (sextet) provided that it has long range order (i.e. large particle size) (Murad, 1982), while spectra corresponding to goethite with short range ordering (i.e. nano-goethite, $d < 20$ nm) are typically dominated by superparamagnetic doublets (van der Kraan and van Loef, 1966). The room temperature Mössbauer spectra recorded for the minerals produced by SW2 with and without additional metals are dominated by a doublet. Coupled with the broad reflections observed in µXRD, it is likely that these goethite minerals are therefore nanoparticulate (van der Zee et al., 2003).

The spectra recorded at 77 K are dominated by a well defined sextet (Gt) and a collapsed sextet corresponding to paramagnetic goethite (para. Gt), which suggests differences between the crystallinity or particle size of the mineral phases present. The relative area of the collapsed sextets are similar in samples without additions and in samples amended with either Ni^{2+}, Zn^{2+} or Hg^{2+}. Samples with Cu^{2+} required the use of a doublet in addition to a collapsed sextet in order to fully fit the sample, suggesting that it is less crystalline or has a smaller particle size than the other samples. The mineral produced in the presence of Ni^{2+} shows a somewhat more complex size dependent effect. For instance, the room temperature measurements show no paramagnetic goethite with only a doublet required to obtain an accurate fit. At 77 K the sample amended with Ni^{2+} showed similar magnetic ordering as compared to the other samples, and yet it is still not fully magnetically ordered at 4.2 K. This likely indicates a broad size distribution of nanogoethite in the samples amended with Ni^{2+}.

The substitution of Fe by elements such as Ni, Al and Si in goethite has previously been reported (Murad and Schwertmann, 1983; de Carvalho-e-Silva et al., 2002), with each case leading to a decrease in the reported hyperfine field with increasing substitution. Examination of the 4.2 K data show little to no differences between the hyperfine fields of each of the goethite samples measured here. This suggests that there has been no significant substitution of any metals into the goethite mineral structure. Therefore, it seems that the most significant impact of the presence of metals in goethite formation is on the crystallinity or particle size.

5. CONCLUSIONS

Using CLSM in combination with metal-specific fluorescent probes as an *in-situ* technique allowed us to investigate the spatial heterogeneity of metal binding to complex systems such as cell-EPS-Fe(III)-mineral aggregates formed by Fe(II)-oxidizing bacteria on the sub-µm scale. The present study linked the observed distribution patterns of metals associated with cells, glycoconjugates and minerals to microbial activity, and to the resulting geochemical microenvironments. The fractions of metals that are sorbed onto cell surfaces, within glycoconjugates and onto mineral surfaces, but that are not incorporated into the (bio-) mineral structure, are relatively mobile and can be expected to be readily biotoxic. The statistical analysis of the

spatially resolved datasets allows us to draw the conclusion that metal binding was relatively similar for all metals studied, namely that Au^{3+}, Cd^{2+}, Cr^{3+}, CrO_4^{2-}, Cu^{2+}, Hg^{2+}, Ni^{2+}, Pd^{2+}, TBT and Zn^{2+}, were heavily affected by the presence of Fe^{2+} and Fe^{3+} iron, which compete for sorption sites on cell surfaces and glycoconjugates in the system. The results of this study showed that in this complex system both bacterial cells and glycoconjugates provided significant amounts of sorption sites for heavy metal species. Simultaneously, microbially formed Fe(III) minerals interaction with glycoconjugate matrices of cell-EPS-Fe(III)-minerals aggregates and provided additional binding sites, whereas Fe^{2+} and Fe^{3+} ions competed with heavy metals for sorption sites on the organic components. Thus, microbial Fe(II) oxidation is not only an important process determining the spatial distribution of iron species but also controls the distribution of heavy metals. The approach developed for this study allows for mapping at high resolution and *in-situ* the local 3D metal distribution. Samples are analyzed in their natural hydrated states and correlation analysis of the resulting 3D analytical datasets allows for identifying relationships between heavy metal species, Fe^{2+} and Fe^{3+} ions, cells, glycoconjugates and biogenic minerals. The information obtained by this relatively novel technique turned out to be very complementary to the information obtained by conventional approaches. It provides important information to understand the interaction mechanisms between heavy metal species and biofilms, the fate of heavy metals, and interaction mechanisms between microbially formed Fe(III) minerals and heavy metals in natural complex environments.

APPENDIX A. SUPPLEMENTARY DATA

Supplementary data associated with this article can be found, in the online version, at http://dx.doi.org/10.1016/j.gca.2016.02.016.

REFERENCES

Abebe F. A., Eribal C. S., Ramakrishna G. and Sinn E. (2011) A 'turn-on' fluorescent sensor for the selective detection of cobalt and nickel ions in aqueous media. *Tetrahedron Lett.* **52**, 5554–5558.

Abramoff M. D. (2004) Image processing with ImageJ. *Biophoton. Int.* **11**, 36–42.

Adler J. and Parmryd I. (2010) Quantifying colocalization by correlation: the Pearson correlation coefficient is superior to the Mander's overlap coefficient. *Cytometry A* **77A**, 733–742.

Appelo C. A. J. and Postma D. (2005) *Geochemistry, Groundwater and Pollution*, second ed. CRC Press.

Ba L. A., Doering M., Burkholz T. and Jacob C. (2009) Metal trafficking: from maintaining the metal homeostasis to future drug design. *Metallomics* **1**, 292–311.

Banin E., Vasil M. L. and Greenberg E. P. (2005) Iron and *Pseudomonas aeruginosa* biofilm formation. *Proc. Natl. Acad. Sci.* **102**, 11076–11081.

Barlow A. L., MacLeod A., Noppen S., Sanderson J. and Guérin C. J. (2010) Colocalization analysis in fluorescence micrographs: verification of a more accurate calculation of Pearson's correlation coefficient. *Microsc. Microanal.* **16**, 710–724.

Bar-Zeev E., Zodrow K. R., Kwan S. E. and Elimelech M. (2014) The importance of microscopic characterization of membrane biofilms in an unconfined environment. *Desalination* **348**, 8–15.

Beija M., Afonso C. A. M. and Martinho J. M. G. (2009) Synthesis and applications of Rhodamine derivatives as fluorescent probes. *Chem. Soc. Rev.* **38**, 2410–2433.

Berthold C., Bjeoumikhov A. and Brügemann L. (2009) Fast XRD² microdiffraction with focusing X-ray microlenses. *Part. Part. Syst. Charact.* **26**, 107–111.

Bird L. J., Coleman M. L. and Newman D. K. (2013) Iron and copper act synergistically to delay anaerobic growth in bacteria. *Appl. Environ. Microbiol.*

Bolte S. and Cordelieres F. P. (2006) A guided tour into subcellular colocalization analysis in light microscopy. *J. Microsc.* **224**, 213–232.

Boyd P. W. and Ellwood M. J. (2010) The biogeochemical cycle of iron in the ocean. *Nat. Geosci.* **3**, 675–682.

Bridier A. and Briandet R. (2014) Contribution of confocal laser scanning microscopy in deciphering biofilm tridimensional structure and reactivity. In *Microbial Biofilms: Methods and Protocols, Methods in Molecular Biology* (ed. G. Donelli). Springer, New York, pp. 255–266.

Buchholz F., Lerchner J., Mariana F., Kuhlicke U., Neu T. R., Harms H. and Maskow T. (2012) Chip-calorimetry provides real time insights into the inactivation of biofilms by predatory bacteria. *Biofouling* **28**, 351–362.

Carter K. P., Young A. M. and Palmer A. E. (2014) Fluorescent sensors for measuring metal ions in living systems. *Chem. Rev.* **114**, 4564–4601.

Chan C. S., De Stasio G., Welch S. A., Girasole M., Frazer B. H., Nesterova M. V., Fakra S. and Banfield J. F. (2004) Microbial polysaccharides template assembly of nanocrystal fibers. *Science* **303**, 1656–1658.

Chang H. T. and Rittmann B. E. (1986) Biofilm loss during sample preparation for scanning electron microscopy. *Water Res.* **20**, 1451–1456.

Chen M.-Y., Lee D.-J., Yang Z., Peng X. F. and Lai J. Y. (2006) Fluorescent staining for study of extracellular polymeric substances in membrane biofouling layers. *Environ. Sci. Technol.* **40**, 6642–6646.

Chen M.-Y., Lee D.-J., Tay J.-H. and Show K.-Y. (2007) Staining of extracellular polymeric substances and cells in bioaggregates. *Appl. Microbiol. Biotechnol.* **75**, 467–474.

Choudhary S. and Sar P. (2009) Characterization of a metal resistant *Pseudomonas* sp. isolated from uranium mine for its potential in heavy metal (Ni^{2+}, Co^{2+}, Cu^{2+}, and Cd^{2+}) sequestration. *Bioresour. Technol.* **100**, 2482–2492.

Clarke S., Mielke R. E., Neal A., Holden P. and Nadeau J. L. (2010) Bacterial and mineral elements in an arctic biofilm: a correlative study using fluorescence and electron microscopy. *Microsc. Microanal.* **16**, 153–165.

Comte S., Guibaud G. and Baudu M. (2006) Biosorption properties of extracellular polymeric substances (EPS) resulting from activated sludge according to their type: soluble or bound. *Process Biochem.* **41**, 815–823.

Comte S., Guibaud G. and Baudu M. (2008) Biosorption properties of extracellular polymeric substances (EPS) towards Cd, Cu and Pb for different pH values. *J. Hazard. Mater.* **151**, 185–193.

Costes S. V., Daelemans D., Cho E. H., Dobbin Z., Pavlakis G. and Lockett S. (2004) Automatic and quantitative measurement of protein-protein colocalization in live cells. *Biophys. J*. **86**, 3993–4003.

Cox J. S., Smith D. S., Warren L. A. and Ferris F. G. (1999) Characterizing heterogeneous bacterial surface functional groups using discrete affinity spectra for proton binding. *Environ. Sci. Technol.* **33**, 4514–4521.

Croal L. R., Jiao Y. and Newman D. K. (2007) The *fox* operon from *Rhodobacter* strain SW2 promotes phototrophic Fe(II) oxidation in *Rhodobacter capsulatus* SB1003. *J. Bacteriol.* **189**, 1774–1782.

Cui Y. and Weng L. (2015) Interpretation of heavy metal speciation in sequential extraction using geochemical modelling. *Environ. Chem.* **12**, 163–173.

d'Abzac P., Bordas F., Joussein E., van Hullebusch E., Lens P. L. and Guibaud G. (2013) Metal binding properties of extracellular polymeric substances extracted from anaerobic granular sludges. *Environ. Sci. Pollut. Res.* **20**, 4509–4519.

Daughney C. J., Fein J. B. and Yee N. (1998) A comparison of the thermodynamics of metal adsorption onto two common bacteria. *Chem. Geol.* **144**, 161–176.

Daughney C. J., Fowle D. A. and Fortin D. (2001) The effect of growth phase on proton and metal adsorption by *Bacillus subtilis*. *Geochim. Cosmochim. Acta* **65**, 1025–1035.

Daughney C. J., Fakih M. and Châtellier X. (2011) Progressive sorption and oxidation/hydrolysis of Fe(II) affects cadmium immobilization by bacteria-iron oxide composites. *Geomicrobiol. J.* **28**, 11–22.

de Carvalho-e-Silva M. L. M., Partiti C. S. M., Enzweiler J., Petit S., Netto S. M. and de Oliveira S. M. B. (2002) Characterization of Ni-containing goethites by Mössbauer spectroscopy and other techniques. *Hyperfine Interact.* **141–142**, 559–576.

Dean K. M., Qin Y. and Palmer A. E. (2012) Visualizing metal ions in cells: an overview of analytical techniques, approaches, and probes. *Biochim. Biophys. Acta* **1823**, 1406–1415.

Denkhaus E., Meisen S., Telgheder U. and Wingender J. (2007) Chemical and physical methods for characterisation of biofilms. *Microchim. Acta* **158**, 1–27.

Dohnalkova A. C., Marshall M. J., Arey B. W., Williams K. H., Buck E. C. and Fredrickson J. K. (2011) Imaging hydrated microbial extracellular polymers: comparative analysis by electron microscopy. *Appl. Environ. Microbiol.* **77**, 1254–1262.

Dzombak D. A. and Morel F. M. M. (1990) *Surface Complexation Modeling: Hydrous Ferric Oxide*. Wiley.

Eickhoff M., Obst M., Schröder C., Hitchcock A. P., Tyliszczak T., Martinez R. E., Robbins L. J., Konhauser K. O. and Kappler A. (2014) Nickel partitioning in biogenic and abiogenic ferrihydrite: the influence of silica and implications for ancient environments. *Geochim. Cosmochim. Acta* **140**, 65–79.

Elliott A. V. C., Plach J. M., Droppo I. G. and Warren L. A. (2012) Comparative floc-bed sediment trace element partitioning across variably contaminated aquatic ecosystems. *Environ. Sci. Technol.* **46**, 209–216.

Elliott A. V. C., Plach J. M., Droppo I. G. and Warren L. A. (2014) Collaborative microbial Fe-redox cycling by pelagic floc bacteria across wide ranging oxygenated aquatic systems. *Chem. Geol.* **366**, 90–102.

Fang L., Cai P., Chen W., Liang W., Hong Z. and Huang Q. (2009) Impact of cell wall structure on the behavior of bacterial cells in the binding of copper and cadmium. *Colloids Surf., A* **347**, 50–55.

Fang L., Yang S., Huang Q., Xue A. and Cai P. (2014) Biosorption mechanisms of Cu(II) by extracellular polymeric substances from *Bacillus subtilis*. *Chem. Geol.* **386**, 143–151.

Faraldo-Gomez J. D. and Sansom M. S. P. (2003) Acquisition of siderophores in gram-negative bacteria. *Nat. Rev. Mol. Cell Biol.* **4**, 105–116.

Fein J. B., Martin A. M. and Wightman P. G. (2001) Metal adsorption onto bacterial surfaces: development of a predictive approach. *Geochim. Cosmochim. Acta* **65**, 4267–4273.

Finney L. A. and O'Halloran T. V. (2003) Transition metal speciation in the cell: insights from the chemistry of metal ion receptors. *Science* **300**, 931–936.

Fischer L., Brümmer G. W. and Barrow N. J. (2007) Observations and modelling of the reactions of 10 metals with goethite: adsorption and diffusion processes. *Eur. J. Soil Sci.* **58**, 1304–1315.

Francis A. J. and Dodge C. J. (1990) Anaerobic microbial remobilization of toxic metals coprecipitated with iron oxide. *Environ. Sci. Technol.* **24**, 373–378.

Gabriel K. R. (1971) The biplot graphic display of matrices with application to principal component analysis. *Biometrika* **58**, 453–467.

Geesey G. G., Borch T. and Reardon C. L. (2008) Resolving biogeochemical phenomena at high spatial resolution through electron microscopy. *Geobiology* **6**, 263–269.

Goyal N., Jain S. C. and Banerjee U. C. (2003) Comparative studies on the microbial adsorption of heavy metals. *Adv. Environ. Res.* **7**, 311–319.

Guibaud G., Tixier N., Bouju A. and Baudu M. (2003) Relation between extracellular polymers' composition and its ability to complex Cd, Cu and Pb. *Chemosphere* **52**, 1701–1710.

Guibaud G., Comte S., Bordas F., Dupuy S. and Baudu M. (2005) Comparison of the complexation potential of extracellular polymeric substances (EPS), extracted from activated sludges and produced by pure bacteria strains, for cadmium, lead and nickel. *Chemosphere* **59**, 629–638.

Guine V., Spadini L., Sarret G., Muris M., Delolme C., Gaudet J. P. and Martins J. M. F. (2006) Zinc sorption to three gram-negative bacteria: combined titration, modeling, and EXAFS study. *Environ. Sci. Technol.* **40**, 1806–1813.

Gupta R., Ahuja P., Khan S., Saxena R. and Mohapatra H. (2000) Microbial biosorbents: meeting challenges of heavy metal pollution in aqueous solutions. *Curr. Sci.* **78**, 967–973.

Haferburg G. and Kothe E. (2012) Biogeosciences in heavy metal-contaminated soils. In *Bio-Geo Interactions in Metal-Contaminated Soils, Soil Biology* (eds. E. Kothe and A. Varma). Springer, Berlin Heidelberg, pp. 17–34.

Halan B., Buehler K. and Schmid A. (2012) Biofilms as living catalysts in continuous chemical syntheses. *Trends Biotechnol.* **30**, 453–465.

Han Z.-X., Zhang X.-B., Zhuo L., Gong Y.-J., Wu X.-Y., Zhen J., He C.-M., Jian L.-X., Jing Z., Shen G.-L. and Yu R.-Q. (2010) Efficient fluorescence resonance energy transfer-based ratiometric fluorescent cellular imaging probe for Zn^{2+} using a Rhodamine spirolactam as a trigger. *Anal. Chem.* **82**, 3108–3113.

Hansel C. M., Benner S. G. and Fendorf S. (2005) Competing Fe (II)-induced mineralization pathways of ferrihydrite. *Environ. Sci. Technol.* **39**, 7147–7153.

Hao L., Li J., Kappler A. and Obst M. (2013) Mapping of heavy metal ion sorption to cell-extracellular polymeric substance-mineral aggregates by using metal-selective fluorescent probes and confocal laser scanning microscopy. *Appl. Environ. Microbiol.* **79**, 6524–6534.

Hegler F., Posth N. R., Jiang J. and Kappler A. (2008) Physiology of phototrophic iron(II)-oxidizing bacteria: implications for modern and ancient environments. *FEMS Microbiol. Ecol.* **66**, 250–260.

Hegler F., Schmidt C., Schwarz H. and Kappler A. (2010) Does a low-pH microenvironment around phototrophic Fe^{II}-oxidizing bacteria prevent cell encrustation by Fe^{III} minerals? *FEMS Microbiol. Ecol.* **74**, 592–600.

Hidalgo G., Burns A., Herz E., Hay A. G., Houston P. L., Wiesner U. and Lion L. W. (2009) Functional tomographic fluorescence imaging of pH microenvironments in microbial biofilms by use of silica nanoparticle sensors. *Appl. Environ. Microbiol.* **75**, 7426–7435.

Hong X.-Q., Li R.-Z., Liu W.-J., Zhang X.-S., Ding H.-S. and Jiang H. (2012) An investigation on reuse of Cr-contaminated sediment: Cr removal and interaction between Cr and organic matter. *Chem. Eng. J.* **189–190**, 222–228.

Hu Z. Q., Hidalgo G., Houston P. L., Hay A. G., Shuler M. L., Abruna H. D., Ghiorse W. C. and Lion L. W. (2005) Determination of spatial distributions of zinc and active biomass in microbial biofilms by two-photon laser scanning microscopy. *Appl. Environ. Microbiol.* **71**, 4014–4021.

Hunter R. C. and Beveridge T. J. (2005) Application of a pH-sensitive fluoroprobe (C-SNARF-4) for pH microenvironment analysis in *Pseudomonas aeruginosa* biofilms. *Appl. Environ. Microbiol.* **71**, 2501–2510.

Jaskolski F., Mulle C. and Manzoni O. J. (2005) An automated method to quantify and visualize colocalized fluorescent signals. *J. Neurosci. Methods* **146**, 42–49.

Jin J. and Guan Y. (2014) The mutual co-regulation of extracellular polymeric substances and iron ions in biocorrosion of cast iron pipes. *Bioresour. Technol.* **169**, 387–394.

Jin X., Hao L., She M., Obst M., Kappler A., Yin B., Liu P., Li J., Wang L. and Shi Z. (2015) Visualizing tributyltin (TBT) in bacterial aggregates by specific rhodamine-based fluorescent probes. *Anal. Chim. Acta* **853**, 514–520.

Julien C., Laurent E., Legube B., Thomassin J. H., Mondamert L. and Labanowski J. (2014) Investigation on the iron-uptake by natural biofilms. *Water Res.* **50**, 212–220.

Jung Jou M., Chen X., Swamy K. M. K., Na Kim H., Kim H.-J., Lee S.-G. and Yoon J. (2009) Highly selective fluorescent probe for Au3+ based on cyclization of propargylamide. *Chem. Commun.*

Kappler A. and Newman D. K. (2004) Formation of Fe(III)-minerals by Fe(II)-oxidizing photoautotrophic bacteria. *Geochim. Cosmochim. Acta* **68**, 1217–1226.

Kappler A., Johnson C. M., Crosby H. A., Beard B. L. and Newman D. K. (2010) Evidence for equilibrium iron isotope fractionation by nitrate-reducing iron(II)-oxidizing bacteria. *Geochim. Cosmochim. Acta* **74**, 2826–2842.

Karamalidis A. K. and Dzombak D. A. (2011) *Surface Complexation Modeling: Gibbsite*. Wiley.

Kemner K. M., O'Loughlin E. J., Kelly S. D. and Boyanov M. I. (2005) Synchrotron X-ray investigations of mineral–microbe–metal interactions. *Elements* **1**, 217–221.

Klueglein N. and Kappler A. (2013) Abiotic oxidation of Fe(II) by reactive nitrogen species in cultures of the nitrate-reducing Fe

(II) oxidizer *Acidovorax* sp. BoFeN1 – questioning the existence of enzymatic Fe(II) oxidation. *Geobiology* **11**, 180–190.

Ko S.-K., Yang Y.-K., Tae J. and Shin I. (2006) In vivo monitoring of mercury ions using a rhodamine-based molecular probe. *J. Am. Chem. Soc.* **128**, 14150–14155.

Kulczycki E., Ferris F. G. and Fortin D. (2002) Impact of cell wall structure on the behavior of bacterial cells as sorbents of cadmium and lead. *Geomicrobiol. J.* **19**, 553–565.

Kumar M., Kumar N. and Bhalla V. (2011) FRET-induced nanomolar detection of Fe^{2+} based on cinnamaldehyde-rhodamine derivative. *Tetrahedron Lett.* **52**, 4333–4336.

Lack J. G., Chaudhuri S. K., Kelly S. D., Kemner K. M., O'Connor S. M. and Coates J. D. (2002) Immobilization of radionuclides and heavy metals through anaerobic bio-oxidation of Fe(II). *Appl. Environ. Microbiol.* **68**, 2704–2710.

Lagarec K. and Rancourt D. G. (1997) Extended Voigt-based analytic lineshape method for determining *N*-dimensional correlated hyperfine parameter distributions in Mössbauer spectroscopy. *Nucl. Instrum. Methods Phys. Res., Sect. B* **129**, 266–280.

Larese-Casanova P., Haderlein S. B. and Kappler A. (2010) Biomineralization of lepidocrocite and goethite by nitrate-reducing Fe(II)-oxidizing bacteria: effect of pH, bicarbonate, phosphate, and humic acids. *Geochim. Cosmochim. Acta* **74**, 3721–3734.

Lawrence J. R., Chenier M. R., Roy R., Beaumier D., Fortin N., Swerhone G. D. W., Neu T. R. and Greer C. W. (2004) Microscale and molecular assessment of impacts of nickel, nutrients, and oxygen level on structure and function of river biofilm communities. *Appl. Environ. Microbiol.* **70**, 4326–4339.

Li W.-W. and Yu H.-Q. (2014) Insight into the roles of microbial extracellular polymer substances in metal biosorption. *Bioresour. Technol.* **160**, 15–23.

Li H., Fan J., Du J., Guo K., Sun S., Liu X. and Peng X. (2010) A fluorescent and colorimetric probe specific for palladium detection. *Chem. Commun.* **46**, 1079–1081.

Li P., Fang L., Zhou H., Zhang W., Wang X., Li N., Zhong H. and Tang B. (2011) A new ratiometric fluorescent probe for detection of Fe^{2+} with high sensitivity and its intracellular imaging applications. *Chem. – Eur. J.* **17**, 10520–10523.

Liu Y. and Xu H. (2007) Equilibrium, thermodynamics and mechanisms of Ni^{2+} biosorption by aerobic granules. *Biochem. Eng. J.* **35**, 174–182.

Loukidou M. X., Zouboulis A. I., Karapantsios T. D. and Matis K. A. (2004) Equilibrium and kinetic modeling of chromium (VI) biosorption by *Aeromonas caviae*. *Colloids Surf., A* **242**, 93–104.

Lu W.-Y., Zhang T., Zhang D.-Y., Li C.-H., Wen J.-P. and Du L.-X. (2005) A novel bioflocculant produced by *Enterobacter aerogenes* and its use in defecating the trona suspension. *Biochem. Eng. J.* **27**, 1–7.

Malkusch S., Endesfelder U., Mondry J., Gelléri M., Verveer P. and Heilemann M. (2012) Coordinate-based colocalization analysis of single-molecule localization microscopy data. *Histochem. Cell Biol.* **137**, 1–10.

Marx V. (2013) Is super-resolution microscopy right for you? *Nat. Methods* **10**, 1157–1163.

McCall K. A. and Fierke C. A. (2000) Colorimetric and fluorimetric assays to quantitate micromolar concentrations of transition metals. *Anal. Biochem.* **284**, 307–315.

McLean J. S., Ona O. N. and Majors P. D. (2008) Correlated biofilm imaging, transport and metabolism measurements via combined nuclear magnetic resonance and confocal microscopy. *ISME J.* **2**, 121–131.

Mikutta R., Baumgärtner A., Schippers A., Haumaier L. and Guggenberger G. (2012) Extracellular polymeric substances from *Bacillus subtilis* associated with minerals modify the extent and rate of heavy metal sorption. *Environ. Sci. Technol.* **46**, 3866–3873.

Miot J., Benzerara K., Obst M., Kappler A., Hegler F., Schaedler S., Bouchez C., Guyot F. and Morin G. (2009) Extracellular iron biomineralization by photoautotrophic iron-oxidizing bacteria. *Appl. Environ. Microbiol.* **75**, 5586–5591.

Mishra B., Boyanov M., Bunker B. A., Kelly S. D., Kemner K. M. and Fein J. B. (2010) High- and low-affinity binding sites for Cd on the bacterial cell walls of *Bacillus subtilis* and *Shewanella oneidensis*. *Geochim. Cosmochim. Acta* **74**, 4219–4233.

More T. T., Yadav J. S. S., Yan S., Tyagi R. D. and Surampalli R. Y. (2014) Extracellular polymeric substances of bacteria and their potential environmental applications. *J. Environ. Manage.* **144**, 1–25.

Morel F. M. M. and Price N. M. (2003) The biogeochemical cycles of trace metals in the oceans. *Science* **300**, 944–947.

Mullen M. D., Wolf D. C., Ferris F. G., Beveridge T. J., Flemming C. A. and Bailey G. W. (1989) Bacterial sorption of heavy metals. *Appl. Environ. Microbiol.* **55**, 3143–3149.

Murad E. (1982) The characterization of goethite by Mössbauer spectroscopy. *Am. Mineral.* **67**, 1007–1011.

Murad E. (2010) Mössbauer spectroscopy of clays, soils and their mineral constituents. *Clay Miner.* **45**, 413–430.

Murad E. and Schwertmann U. (1983) The influence of aluminium substitution and crystallinity on the Mössbauer spectra of goethite. *Clay Miner.* **18**, 301–312.

Nagano T. (2010) Development of fluorescent probes for bioimaging applications. *Proc. Jpn Acad. Ser. B* **86**, 837–847.

Neu T. R. and Lawrence J. R. (1999) Lectin-binding analysis in biofilm systems. In *Methods in Enzymology* (ed. J. D. Ron). Academic Press, pp. 145–152.

Neu T. R. and Lawrence J. R. (2003) *Laser Scanning Microscopy in Combination with Fluorescence Techniques for Biofilm Study. Encyclopedia of Environmental Microbiology*. John Wiley & Sons Inc., pp. 1772–1788.

Neu T. and Lawrence J. (2014a) Advanced techniques for in situ analysis of the biofilm matrix (structure, composition, dynamics) by means of laser scanning microscopy. In *Microbial Biofilms: Methods and Protocols, Methods in Molecular Biology* (ed. G. Donelli). Springer, New York, pp. 43–64.

Neu T. and Lawrence J. (2014b) *Investigation of microbial biofilm structure by laser scanning microscopy*. Springer, Berlin Heidelberg, pp. 1–51.

Nguyen T. and Francis M. B. (2003) Practical synthetic route to functionalized rhodamine dyes. *Org. Lett.* **5**, 3245–3248.

Nieboer E. and Richardson D. H. S. (1980) The replacement of the nondescript term 'heavy metals' by a biologically and chemically significant classification of metal ions. *Environ. Poll. Ser. B, Chem. Phys.* **1**, 3–26.

Pacyna E. G., Pacyna J. M., Fudala J., Strzelecka-Jastrzab E., Hlawiczka S., Panasiuk D., Nitter S., Pregger T., Pfeiffer H. and Friedrich R. (2007) Current and future emissions of selected heavy metals to the atmosphere from anthropogenic sources in Europe. *Atmos. Environ.* **41**, 8557–8566.

Penner-Hahn J. (2013) Technologies for detecting metals in single cells. In *Metallomics and the Cell* (ed. L. Banci). Springer, Netherlands, pp. 15–40.

Plach J. M., Elliott A. V. C., Droppo I. G. and Warren L. A. (2011) Physical and ecological controls on freshwater Floc trace metal dynamics. *Environ. Sci. Technol.* **45**, 2157–2164.

Plette A. C. C., Benedetti M. F. and van Riemsdijk W. H. (1996) Competitive binding of protons, calcium, cadmium, and zinc to isolated cell walls of a Gram-positive soil bacterium. *Environ. Sci. Technol.* **30**, 1902–1910.

Pokrovsky O. S., Viers J., Emnova E. E., Kompantseva E. I. and Freydier R. (2008) Copper isotope fractionation during its interaction with soil and aquatic microorganisms and metal oxy (hydr)oxides: possible structural control. *Geochim. Cosmochim. Acta* **72**, 1742–1757.

Posth N. R., Canfield D. E. and Kappler A. (2014) Biogenic Fe(III) minerals: from formation to diagenesis and preservation in the rock record. *Earth Sci. Rev.* **135**, 103–121.

Ravichandran M. (2004) Interactions between mercury and dissolved organic matter—a review. *Chemosphere* **55**, 319–331.

Reuben S., Banas K., Banas A. and Swarup S. (2014) Combination of synchrotron radiation-based Fourier transforms infrared microspectroscopy and confocal laser scanning microscopy to understand spatial heterogeneity in aquatic multispecies biofilms. *Water Res.* **64**, 123–133.

Rosivatz E. (2008) Imaging the boundaries—innovative tools for microscopy of living cells and real-time imaging. *J. Chem. Biol.* **1**, 3–15.

Sar P., Kazy S. K. and Singh S. P. (2001) Intracellular nickel accumulation by *Pseudomonas aeruginosa* and its chemical nature. *Lett. Appl. Microbiol.* **32**, 257–261.

Schädler S., Burkhardt C. and Kappler A. (2008) Evaluation of electron microscopic sample preparation methods and imaging techniques for characterization of cell-mineral aggregates. *Geomicrobiol. J.* **25**, 228–239.

Schädler S., Burkhardt C., Hegler F., Straub K. L., Miot J., Benzerara K. and Kappler A. (2009) Formation of cell-iron-mineral aggregates by phototrophic and nitrate-reducing anaerobic Fe(II)-oxidizing bacteria. *Geomicrobiol. J.* **26**, 93–103.

Schmid G., Zeitvogel F., Hao L., Ingino P., Floetenmeyer M., Stierhof Y. D., Schroeppel B., Burkhardt C. J., Kappler A. and Obst M. (2014) 3-D analysis of bacterial cell-(iron) mineral aggregates formed during Fe(II) oxidation by the nitrate-reducing *Acidovorax* sp. strain BoFeN1 using complementary microscopy tomography approaches. *Geobiology* **12**, 340–361.

She M., Yang Z., Yin B., Zhang J., Gu J., Yin W., Li J., Zhao G. and Shi Z. (2012) A novel rhodamine-based fluorescent and colorimetric "off–on" chemosensor and investigation of the recognizing behavior towards Fe^{3+}. *Dyes Pigm.* **92**, 1337–1343.

Sheng G.-P. and Yu H.-Q. (2006) Relationship between the extracellular polymeric substances and surface characteristics of *Rhodopseudomonas acidophila*. *Appl. Microbiol. Biotechnol.* **72**, 126–131.

Shumi W., Lim J., Nam S.-W., Kim S. H., Cho K.-S., Yoon J. and Park S. (2009) Fluorescence imaging of the spatial distribution of ferric ions over biofilms formed by *Streptococcus mutans* under microfluidic conditions. *Biochip. J.* **3**, 119–124.

Shumi W., Lim J., Nam S.-W., Lee K., Kim S., Kim M.-H., Cho K.-S. and Park S. (2010) Environmental factors that affect *Streptococcus mutans* biofilm formation in a microfluidic device mimicking teeth. *BioChip J.* **4**, 257–263.

Singh P. K., Parsek M. R., Greenberg E. P. and Welsh M. J. (2002) A component of innate immunity prevents bacterial biofilm development. *Nature* **417**, 552–555.

Späth R., Flemming H. C. and Wuertz S. (1998) Sorption properties of biofilms. *Water Sci. Technol.* **37**, 207–210.

Srinath T., Verma T., Ramteke P. W. and Garg S. K. (2002) Chromium (VI) biosorption and bioaccumulation by chromate resistant bacteria. *Chemosphere* **48**, 427–435.

Staudt C., Horn H., Hempel D. C. and Neu T. R. (2004) Volumetric measurements of bacterial cells and extracellular polymeric substance glycoconjugates in biofilms. *Biotechnol. Bioeng.* **88**, 585–592.

Sterritt R. M. and Lester J. N. (1980) Interactions of heavy metals with bacteria. *Sci. Total Environ.* **14**, 5–17.

Suter D., Siffert C., Sulzberger B. and Stumm W. (1988) Catalytic dissolution of iron(III)(hydr)oxides by oxalic acid in the presence of Fe(II). *Naturwissenschaften* **75**, 571–573.

Swanner E. D., Wu W., Schoenberg R., Byrne J., Michel F. M., Pan Y. and Kappler A. (2015) Fractionation of Fe isotopes during Fe(II) oxidation by a marine photoferrotroph is controlled by the formation of organic Fe-complexes and colloidal Fe fractions. *Geochim. Cosmochim. Acta* **165**, 44–61.

Takahashi A., Camacho P., Lechleiter J. D. and Herman B. (1999) Measurement of intracellular calcium. *Physiol. Rev.* **79**, 1089–1125.

Teitzel G. M. and Parsek M. R. (2003) Heavy metal resistance of biofilm and planktonic *Pseudomonas aeruginosa*. *Appl. Environ. Microbiol.* **69**, 2313–2320.

Templeton A. and Knowles E. (2009) Microbial transformations of minerals and metals: recent advances in geomicrobiology derived from synchrotron-based X-ray spectroscopy and X-ray microscopy. *Annu. Rev. Earth Planet. Sci.* **37**, 367–391.

Toner B., Manceau A., Marcus M. A., Millet D. B. and Sposito G. (2005) Zinc sorption by a bacterial biofilm. *Environ. Sci. Technol.* **39**, 8288–8294.

Tourney J. and Ngwenya B. T. (2014) The role of bacterial extracellular polymeric substances in geomicrobiology. *Chem. Geol.* **386**, 115–132.

Ueshima M., Ginn B. R., Haack E. A., Szymanowski J. E. S. and Fein J. B. (2008) Cd adsorption onto *Pseudomonas putida* in the presence and absence of extracellular polymeric substances. *Geochim. Cosmochim. Acta* **72**, 5885–5895.

Valls M. and de Lorenzo V. (2002) Exploiting the genetic and biochemical capacities of bacteria for the remediation of heavy metal pollution. *FEMS Microbiol. Rev.* **26**, 327–338.

van der Kraan A. M. and van Loef J. J. (1966) Superparamagnetism in submicroscopic α-FeOOH particles observed by the Mössbauer effect. *Phys. Lett.* **20**, 614–616.

van der Zee C., Roberts D. R., Rancourt D. G. and Slomp C. P. (2003) Nanogoethite is the dominant reactive oxyhydroxide phase in lake and marine sediments. *Geology* **31**, 993–996.

van Hullebusch E. D., Peerbolte A., Zandvoort M. H. and Lens P. N. L. (2005) Sorption of cobalt and nickel on anaerobic granular sludges: isotherms and sequential extraction. *Chemosphere* **58**, 493–505.

Vendrell M., Zhai D., Er J. C. and Chang Y.-T. (2012) Combinatorial strategies in fluorescent probe development. *Chem. Rev.* **112**, 4391–4420.

Wagner M., Ivleva N. P., Haisch C., Niessner R. and Horn H. (2009) Combined use of confocal laser scanning microscopy (CLSM) and Raman microscopy (RM): investigations on EPS – matrix. *Water Res.* **43**, 63–76.

Wagner M., Manz B., Volke F., Neu T. R. and Horn H. (2010a) Online assessment of biofilm development, sloughing and forced detachment in tube reactor by means of magnetic resonance microscopy. *Biotechnol. Bioeng.* **107**, 172–181.

Wagner M., Taherzadeh D., Haisch C. and Horn H. (2010b) Investigation of the mesoscale structure and volumetric features of biofilms using optical coherence tomography. *Biotechnol. Bioeng.* **107**, 844–853.

Wang Y., Wilks J. C., Danhorn T., Ramos I., Croal L. and Newman D. K. (2011) Phenazine-1-carboxylic acid promotes bacterial biofilm development via ferrous iron acquisition. *J. Bacteriol.* **193**, 3606–3617.

Warren L. A. and Ferris F. G. (1998) Continuum between sorption and precipitation of Fe(III) on microbial surfaces. *Environ. Sci. Technol.* **32**, 2331–2337.

Warren L. A. and Haack E. A. (2001) Biogeochemical controls on metal behaviour in freshwater environments. *Earth Sci. Rev.* **54**, 261–320.

L. Hao et al. / Geochimica et Cosmochimica Acta 180 (2016) 66–96

Waychunas G., Kim C. and Banfield J. (2005) Nanoparticulate iron oxide minerals in soils and sediments: unique properties and contaminant scavenging mechanisms. *J. Nanopart. Res.* **7**, 409–433.

Weerasinghe A. J., Schmiesing C. and Sinn E. (2009) Highly sensitive and selective reversible sensor for the detection of Cr^{3+}. *Tetrahedron Lett.* **50**, 6407–6410.

Wessel A. K., Hmelo L., Parsek M. R. and Whiteley M. (2013) Going local: technologies for exploring bacterial microenvironments. *Nat. Rev. Microbiol.* **11**, 337–348.

Witter A. E., Hutchins D. A., Butler A. and Luther Iii G. W. (2000) Determination of conditional stability constants and kinetic constants for strong model Fe-binding ligands in seawater. *Mar. Chem.* **69**, 1–17.

Wu W., Swanner E. D., Hao L., Zeitvogel F., Obst M., Pan Y. and Kappler A. (2014) Characterization of the physiology and cell-mineral interactions of the marine anoxygenic phototrophic Fe(II)-oxidizer *Rhodovulum iodosum* – implications for Precambrian Fe(II) oxidation. *FEMS Microbiol. Ecol.* **88**, 503–515.

Wuertz S., Muller E., Spaeth R., Pfleiderer P. and Flemming H. C. (2000) Detection of heavy metals in bacterial biofilms and microbial flocs with the fluorescent complexing agent Newport Green. *J. Ind. Microbiol. Biotechnol.* **24**, 116–123.

Xi P., Dou J., Huang L., Xu M., Chen F., Wu Y., Bai D., Li W. and Zeng Z. (2010) A selective turn-on fluorescent sensor for Cu(II) and its application in imaging in living cells. *Sens. Actuators. B: Chem.* **148**, 337–341.

Xu L., Xu Y., Zhu W., Sun X., Xu Z. and Qian X. (2012) Modulating the selectivity by switching sensing media: a bifunctional chemosensor selectivity for Cd^{2+} and Pb^{2+} in different aqueous solutions. *RSC Adv.* **2**, 6323–6328.

Yang Y., Zhao Q., Feng W. and Li F. (2012) Luminescent chemodosimeters for bioimaging. *Chem. Rev.* **113**, 192–270.

Yang Z., Hao L., Yin B., She M., Obst M., Kappler A. and Li J. (2013a) Six-membered spirocycle triggered probe for visualizing Hg^{2+} in living cells and bacteria–EPS–mineral aggregates. *Org. Lett.* **15**, 4334–4337.

Yang Z., She M., Zhang J., Chen X., Huang Y., Zhu H., Liu P., Li J. and Shi Z. (2013b) Highly sensitive and selective rhodamine Schiff base "off-on" chemosensors for Cu^{2+} imaging in living cells. *Sens. Actuators, B: Chem.* **176**, 482–487.

Yang Z., She M., Yin B., Hao L., Obst M., Liu P. and Li J. (2015) Solvent-dependent turn-on probe for dual monitoring of Ag^+

and Zn^{2+} in living biological samples. *Anal. Chim. Acta* **868**, 53–59.

Yu M., Shi M., Chen Z., Li F., Li X., Gao Y., Xu J., Yang H., Zhou Z., Yi T. and Huang C. (2008) Highly sensitive and fast responsive fluorescence turn-on chemodosimeter for Cu^{2+} and its application in live cell imaging. *Chem. – Eur. J.* **14**, 6892–6900.

Yu F., Zhang W., Li P., Xing Y., Tong L., Ma J. and Tang B. (2009) Cu^{2+}-selective naked-eye and fluorescent probe: its crystal structure and application in bioimaging. *Analyst* **134**, 1826–1833.

Zeitvogel F., Schmid G., Hao L., Ingino P. and Obst M. (2014) ScatterJ: an ImageJ plugin for the evaluation of analytical microscopy datasets. *J. Microscopy*, n/a–n/a.

Zhang L.-F., Zhao J.-L., Zeng X., Mu L., Jiang X.-K., Deng M., Zhang J.-X. and Wei G. (2011a) Tuning with pH: the selectivity of a new rhodamine B derivative chemosensor for Fe^{3+} and Cu^{2+}. *Sens. Actuators, B: Chem.* **160**, 662–669.

Zhang W., Sileika T. S., Chen C., Liu Y., Lee J. and Packman A. I. (2011b) A novel planar flow cell for studies of biofilm heterogeneity and flow–biofilm interactions. *Biotechnol. Bioeng.* **108**, 2571–2582.

Zheng A., Chen J., Wu G., Wu G., Zhang Y. G. and Wei H. (2009) A novel fluorescent distinguished probe for Cr (VI) in aqueous solution. *Spectrochim. Acta Part A Mol. Biomol. Spectrosc.* **74**, 265–270.

Zheng Y., Xiao Y., Yang Z.-H., Wu S., Xu H.-J., Liang F.-Y. and Zhao F. (2014) The bacterial communities of bioelectrochemical systems associated with the sulfate removal under different pHs. *Process Biochem.* **49**, 1345–1351.

Zhu M., Ginder-Vogel M. and Sparks D. L. (2010) Ni(II) sorption on biogenic Mn-oxides with varying Mn octahedral layer structure. *Environ. Sci. Technol.* **44**, 4472–4478.

Zinchuk V., Wu Y. and Grossenbacher-Zinchuk O. (2013) Bridging the gap between qualitative and quantitative colocalization results in fluorescence microscopy studies. *Sci. Rep.* **3**.

Zippel B. and Neu T. R. (2011) Characterization of glycoconjugates of extracellular polymeric substances in Tufa-associated biofilms by using fluorescence lectin-binding analysis. *Appl. Environ. Microbiol.* **77**, 505–516.

Associate editor: John Moreau